Convectively Driven Turbulent Mixing in the Upper Ocean†

T. J. SHAY* AND M. C. GREGG

Applied Physics Laboratory and School of Oceanography, College of Ocean and Fishery Sciences, University of Washington, Seattle, WA 98105

(Manuscript received 9 December 1985, in final form 4 April 1986)

ABSTRACT

Two experiments were performed to study the characteristics of turbulence in convective mixed layers in the upper ocean. In the first, a diurnal convective mixed layer developed in the Bahamas under the influence of the cycle of daytime solar heating and nighttime evaporative cooling. The mixed layer reached as deep as 100 m each night and restratified each day. In the second, the mixed layer of a warm-core Gulf Stream ring deepened from less than 50 m to more than 150 m in a little more than a day, when subjected to rapid cooling during a cold air outbreak. Although individual profiles of ϵ, the rate of viscous dissipation of turbulent kinetic energy, had considerable spatial and temporal variability, the mean dissipation profiles were similar to those in convecting atmospheric boundary layers. The $\bar{\epsilon}$ is established by the surface buoyancy flux, J_b^0; $\bar{\epsilon}/J_b^0 = 0.61$ and 0.72 in the Bahamas and ring data, respectively, compared with 0.64 in convecting atmospheric mixed layers. The mean profiles decrease gradually, no more than a factor of 3, through the mixed layer and drop abruptly, by 1 to 2 decades, at the mixed layer base.

1. Introduction

Wind stress and surface buoyancy flux supply the energy for turbulent exchange between the ocean and atmosphere. Although wind stress alone can drive mixing in the upper ocean, the deepest oceanic mixed layers are produced by surface cooling, when buoyant production leads to convection. This turbulent mixing process has seldom been studied experimentally in the ocean, and the parameterization of dissipation during convection remains a major unanswered question of mixed layer dynamics (Niiler and Kraus, 1977). Although the turbulence in the atmospheric convective mixed layer is better understood, it is not clear how applicable the results are to the ocean (Thorpe, 1985).

The goal of experimental boundary layer studies is to parameterize turbulence using the surface buoyancy and momentum fluxes and large-scale velocity shear. This approach has been applied with success to the atmospheric convective boundary layer (Businger et al., 1971; Wyngaard, 1983). In fully-developed convection, well away from the surface, the production of turbulent kinetic energy (TKE) by the Reynolds stress becomes small and buoyant production becomes the dominant source of TKE. It is then possible to produce simple relationships predicting the forms of the dissipation rate profiles (Kaimal et al., 1976; Caughey and Palmer, 1979; Guillemet et al., 1983).

There have been fewer experimental studies of turbulence in the oceanic mixed layer. Oakey and Elliott (1982) analyze data from a shallow wind-driven oceanic mixed layer and show that $\bar{\epsilon}$, the mean rate of dissipation of turbulent kinetic energy, is proportional to U_{10}^3 (U_{10} is the wind speed at a height of 10 m). Shay and Gregg (1984a,b) show that $\bar{\epsilon}$ in a deep oceanic convective mixed layer is proportional to the surface buoyancy flux, J_b^0. Imberger (1985) presents similar results in an examination of data from a diurnal mixed layer in a freshwater reservoir.

Two experiments are discussed in this paper. First, the turbulence in a diurnal convective mixed layer observed near the Bahamas is analyzed (Shay and Gregg, 1982). These data display some characteristics of the classic diurnal mixed layer as well as some differences related to disruption of the diurnal heating cycle. Second, a comprehensive analysis of the turbulence in the mixed layer of a Gulf Stream warm core ring during a cold air outbreak is presented. Shay and Gregg (1984a,b) present a preliminary analysis of these data. More details are given here to show the range of variability and to compare the results with the diurnal case.

Section 2 contains a brief description of the instrumentation and data processing (more details are in the Appendix). Specifics of the Bahamas and ring experiments are discussed in sections 3 and 4, respectively. Each section contains discussions of the background oceanographic environment, the meteorological forcing, the hydrographic response to that forcing, and the

† School of Oceanography, University of Washington, Contribution Number 1656.

* Present affiliation: Centre for Environmental Fluid Dynamics, University of Western Australia, Nedlands, Western Australia 6009.

behavior of ϵ. In section 5, the properties of ϵ in the two experiments are compared with each other and with those of atmospheric convective mixed layers. Discussion and conclusions are presented in section 6.

2. Instruments and methods

The purpose of the experiments was to characterize the turbulence during convectively driven mixing and to compare the results with measurements from the atmospheric boundary layer. Although laboratory and atmospheric experiments have been performed in environments chosen to minimize the effects of large-scale velocity shear and horizontal gradients, such conditions are hard to find in the ocean. Since the larger scale environment affects the structure and evolution of the turbulence, the direct turbulence measurements are supplemented with measurements of the hydrographic and velocity fields.

a. Oceanographic data

Vertical profiles of thermohaline finestructure and of temperature and velocity microstructure were made with the Advanced Microstructure Profiler (AMP) (Gregg et al., 1982). The range of fall rates used in the two experiments was 0.45 to 0.80 m s^{-1}. The data for computing ϵ are acquired using two airfoil probes (Osborn and Crawford, 1980). The probes measure the component of velocity fluctuations normal to the direction of the probe's motion, and respond to signals in the dissipation subrange of the kinetic energy spectrum. Standard spectral methods are used to obtain ϵ: the shear spectrum is calculated from 0.5 m sections of data, corrected for sensor and circuit response functions, and then integrated to a cutoff wavenumber. Two methods for choosing the cutoff are compared in the Appendix. Shay (1985) contains a more complete description of the data processing.

The temperature and conductivity channels of AMP are periodically calibrated at sea using a temperature-controlled calibration bath developed by N. Larson (personal communication, 1983). Corrections for drift and offsets are later applied to the data. The precision and accuracy of the temperature measurements are 3 and 10 m°C, respectively. The precision and accuracy of the conductivity measurements are 0.005 S m^{-1} and 0.01 S m^{-1}, respectively. An additional error in the temperature measurements results from pressure distorting the thermistor. This effect varies with the physical characteristics of the probes, but ranges from $(-3$ to $-9) \times 10^{-5}$ °C m^{-1} (J. Carlson, personal communication, 1985); this range corresponds to (0.3 to 1.0) Γ, where Γ is the adiabatic lapse rate. We did not correct for the pressure effect.

Vertical profiles of the large-scale velocity field were occasionally made using Expendable Current Profilers (XCP) (Drever and Sanford, 1980). The XCP does not give the absolute velocity, but vertical shear is considered to be accurate at scales greater than 10 m (Gregg et al., 1986).

b. Meteorological data

The energy driving the turbulent mixing in the upper ocean is provided by the wind stress and the surface heat flux. The energy flux at a height of 10 m, E_{10}, is given by

$$E_{10} = \tau U_{10} \quad [\mathrm{W\,m^{-2}}] \tag{1}$$

where τ is the wind stress and U_{10} is the wind speed at 10 m. It is generally found that a small fraction (about 1 to 2%) of E_{10} is available for mixing in the upper ocean (Denman and Miyake, 1973).

The other source of energy, the surface buoyancy flux, J_b^0, is the surface value of the rate of buoyant production of turbulent kinetic energy. The J_b^0 contains contributions from the surface heat flux, J_q^0, and the surface salt flux, J_s^0:

$$J_b^0 = \frac{-g}{\rho_w}\left[\frac{\alpha}{c_p}J_q^0 + \beta J_s^0\right] = \frac{g}{\rho_w}\left[\frac{-\alpha}{c_p}J_q^0 + \frac{\beta s}{L_E(1-s)}J_q^e\right] \quad [\mathrm{W\,kg^{-1}}] \tag{2}$$

where g is the gravitational acceleration, ρ_w is the density of seawater (1025 kg m^{-3}), α is the coefficient of thermal expansion $[(-2$ to $-2.5) \times 10^{-4}$ $K^{-1}]$, c_p is the specific heat of seawater at constant pressure (4.1×10^3 J K^{-1} kg^{-1}), β is the coefficient of haline contraction (0.76 to 0.81), L_E is the latent heat of evaporation (2.5×10^6 J kg^{-1}), s is salinity expressed as a concentration (e.g., 0.035), and J_q^e is the evaporative heat flux. Positive heat and buoyancy fluxes represent losses from the ocean. The salinity term usually makes a small contribution to J_b^0. For example, if J_q^0 and J_q^e are 300 and 150 W m^{-2}, respectively, then the total buoyancy flux is 1.71×10^{-7} W kg^{-1} and the salinity term is 1.6×10^{-8} W kg^{-1}, only 10% of the total.

In turn, J_q^0 has four components:

$$J_q^0 = J_q^{sw} + J_q^{lw} + J_q^e + J_q^s \quad [\mathrm{W\,m^{-2}}] \tag{3}$$

where J_q^{sw} is the shortwave radiative flux, J_q^{lw} is the longwave radiative flux, and J_q^s is the sensible heat flux. In the Bahamas, measurements of temperature, humidity, wind velocity and radiation were taken every minute by instruments mounted on a spar buoy. For the ring experiment, data recorded every two hours in the ship's weather log were used. In both cases, τ, J_q^s and J_q^e were calculated using bulk aerodynamic formulae and the transfer coefficients given as functions of stability and wind speed by Large and Pond (1981, 1982). Since direct radiation measurements were not available from the ring, bulk formulae were also used for the radiative fluxes (J_q^{sw} and J_q^{lw}) (Smith and Dobson, 1984).

In an existing mixed layer where the only sources of TKE are the wind stress and buoyancy flux, the

Monin-Obukhov length shows the relative contributions of the two sources; it arises simply out of dimensional analysis and is given by,

$$L \equiv \frac{-u_*^3}{\kappa J_b^0} \quad [\mathrm{m}] \tag{4}$$

where u_* is the ocean surface layer friction velocity defined as

$$u_* = \left(\frac{\tau}{\rho_w}\right)^{1/2} \quad [\mathrm{m\,s^{-1}}] \tag{5}$$

and κ is von Karman's constant. As defined, L is negative during conditions favorable to convection ($J_b^0 > 0$). Since u_*^3 is proportional to the input of kinetic energy by the wind and J_b^0 is the buoyant production, L defines a depth at which the two processes are of similar importance for the production of TKE; below L, buoyant production becomes the important source. Thus, in a mixed layer with depth $|D| \gg |L|$, much of the mixed layer should be dominated by convectively driven turbulence (Phillips, 1977). The ratio D/L can therefore be used as a bulk stability parameter indicating the degree of convective instability of the mixed layer. This development relies on the assumption of a smooth surface, and is not a priori applicable to the upper ocean, which contains waves, breaking waves, bubbles and Langmuir cells (Thorpe, 1985). We will test whether L actually indicates the depth below which convection is important in the ocean.

3. Diurnal mixed layer in the Bahamas

a. Background

A diurnal convective mixed layer was observed in the Tongue of the Ocean, Bahamas, in January 1982 (Shay and Gregg, 1982). The Tongue of the Ocean is a narrow (40 to 100 km wide) channel east of Andros Island. The channel is bounded on the west by a narrow shelf, on the east by a broad arm of the Great Bahama Bank, and reaches a maximum depth of 3000 m.

Bursts of AMP drops were made intermittently between 3 and 11 January. Most were made at night during periods of surface cooling. The bursts were clustered within a 10 × 30 km area, but horizontal gradients were strong enough that repositioning usually resulted in shifts in the mean hydrographic properties.

b. Meteorological forcing

Isolated peaks of wind forcing (E_{10}) occurred throughout the experiment, but the mean value of 0.4 W m^{-2} corresponds to a moderate wind speed, 5 m s^{-1} (Fig. 1a). On 10 and 11 January, an increase in E_{10} accompanied the arrival of a cold front.

The air was not more than 2°C cooler than the sea surface until the arrival of a cold front on 10 January. Subsequently, the air–sea temperature difference increased to 5°C on 12 January. The cold front was a precursor of a severe cold air outbreak that froze the Florida citrus crop, but the cruise ended as the outbreak began.

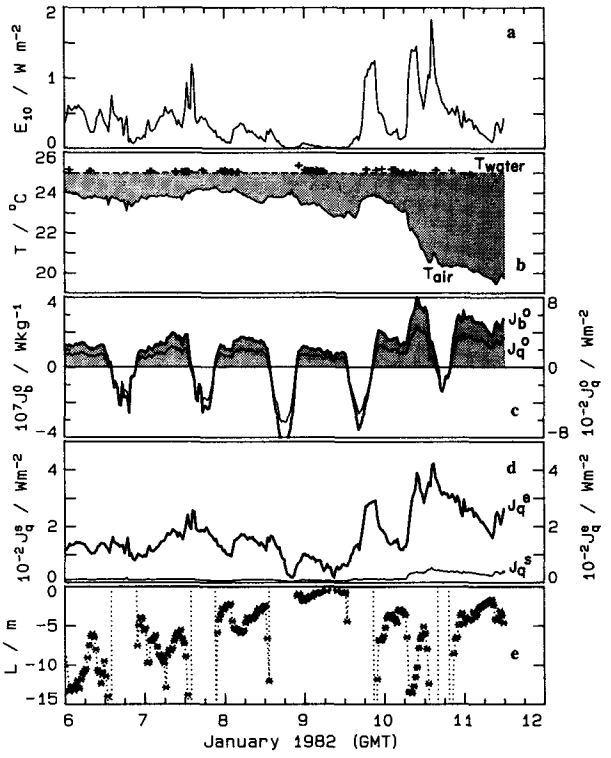

FIG. 1. Thirty-minute averages of the meteorological data from the Bahamas. Local noon is at 1700 GMT. E_{10} is the energy flux produced by the wind stress. A constant water temperature of 25°C (broken line) was used for flux calculations; AMP sea surface temperatures (+) show that this approximation is correct to within 0.2°C (and incidently show the times of AMP drops). J_b^0 (heavy line) is the surface buoyancy flux, and J_q^0 (thin line) is the surface heat flux. Positive fluxes (shaded) represent a loss of heat or buoyancy from the ocean. J_q^e (heavy line) is the evaporative heat flux and J_q^s (thin line) is the sensible heat flux. L (•) is the Monin-Obukhov length; when L is negative, conditions are favorable for convection. The time series of L is shown as a dotted line near sunrise and sunset when J_b^0 passes through zero, and L is ill-defined.

The AMP sea surface temperatures were within 0.2°C of 25°C (+ in Fig. 1b). A constant sea surface temperature of 25°C was used in flux calculations.

The incoming shortwave radiation was dominant during the day, as expected. The peak incoming heat flux reached −400 to −600 W m^{-2} on most days, but cloud cover reduced the peak value to below −300 W m^{-2} on 10 January.

At night, the sensible, evaporative, and outgoing longwave radiative components combined to yield net upward heat (J_q^0) and buoyancy fluxes (J_b^0). (A positive flux is a loss from the ocean.) The surface cooling at night was typically −150 to −200 W m^{-2} before and −300 to −350 W m^{-2} after the arrival of the cold front. Typical values of J_b^0 were (1.0 to 2.0) × 10^{-7} W kg^{-1}

before and (2.5 to 3.0) $\times 10^{-7}$ W kg^{-1} after the arrival of the cold front (Fig. 1c).

The Monin-Obukhov length (L, Fig. 1e) reflects the diurnal cycle of convectively stable ($L > 0$) and convectively unstable ($L < 0$) conditions. During the nighttime periods of unstable conditions, the mixed layer depths (D) ranged from -20 to -90 m while L ranged from -1 to -10 m. The nighttime values of D/L ranged from 2 to 76; these would be interpreted as weakly to moderately convective conditions in the atmospheric boundary layer. We observed convectively driven mixed layer deepening on each of several nights, both before and after the arrival of the cold front.

c. *Hydrographic response*

The behavior of the hydrographic fields can be illustrated with two sets of profiles—one from a daytime drop and one from a nighttime drop, shown in Figs. 2 and 3, respectively. (The gaps near 0.90 MPa in these and other profiles from the Bahamas are a feature of the data acquisition system used for that cruise.) AMP drop 391 (Fig. 2) was taken at 1720 local time 8 January, near sunset. The solar radiation on 8 January was the highest of the cruise and, combined with low winds, resulted in a warm, 10 m thick surface layer. Below the surface layer, a small amount of restratification was caused by the depth-dependent absorption of shortwave radiation. The buoyancy frequency, N, was about 0.01 s^{-1} in the thin surface layer, but then dropped to 0.001 to 0.002 s^{-1} between the surface layer and the top of the seasonal thermocline, where it again increased to about 0.01 s^{-1}.

The relative contributions of the temperature and salinity gradients to the stratification are given by

$$R_\rho = \frac{\beta(\partial s/\partial z)}{\alpha(\partial T/\partial z)}. \tag{6}$$

When $R_\rho < 1$ temperature is more important, and when $R_\rho > 1$ salinity makes the dominant contribution. The quadrant of the gradient T–S diagram (quad) gives the stability of water parcels to double diffusive convection. (Quadrant 1 is unstable to salt fingering; quadrant 2 is diffusively stable; quadrant 3 is unstable to the diffusive mode of double diffusion; and quadrant 4 is gravitationally unstable. Quadrant 0 means that either the temperature or salinity gradient was zero.) This daytime profile has sections in quadrants 1, 2 and 3, but no gravitationally unstable sections. The relative contribution, R_ρ, and the quadrant can be used as indicators of potential double diffusive activity; the double diffusive aspects of these data are discussed elsewhere (Larson and Gregg, 1983). The stratification was

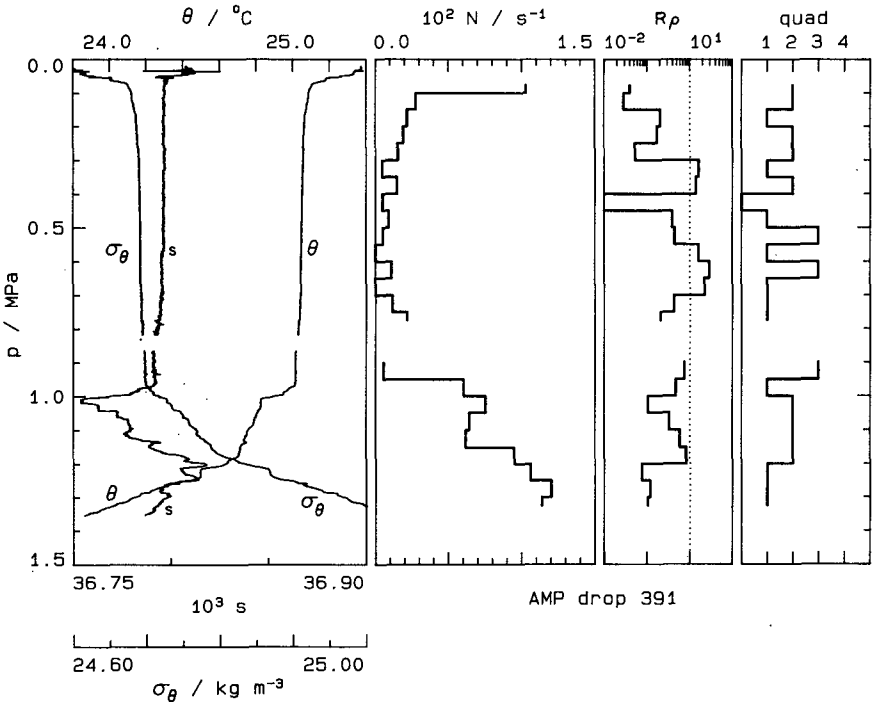

FIG. 2. Representative daytime conditions during the Bahamas experiment. (1 MPa corresponds to 100 m.) The potential temperature (θ), salinity (s) and potential density (σ_θ) are computed from 0.1 m vertical averages. (The gaps were introduced by the data acquisition system.) The buoyancy frequency (N), density ratio (R_ρ), and quadrant (quad) are calculated by first differences across 5 m bins. The absorption of shortwave radiation has warmed the upper 10 m by 0.2°C and restratified the upper ocean.

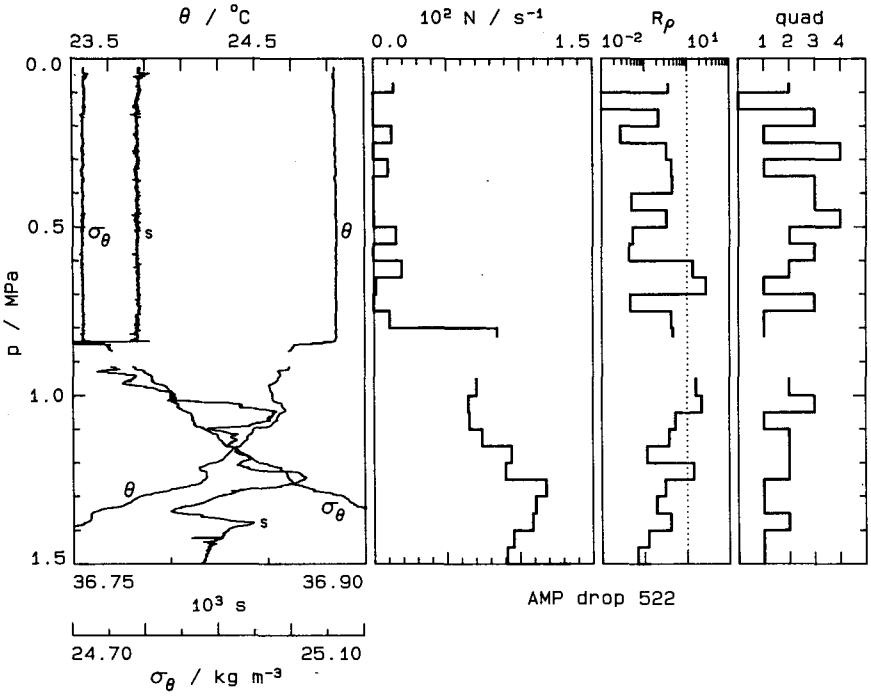

FIG. 3. Representative nighttime conditions during the Bahamas experiment. The format is identical to that in Fig. 2. The water column is well mixed to 0.85 MPa, and the resulting temperature profile is adiabatic within the mixed layer. Gravitational instabilities exist on scales of up to 5 m in the vertical.

mainly controlled by the temperature gradient, although isolated portions of the profiles were salinity-dominated.

The nighttime condition is represented by AMP drop 522 (Fig. 3), taken on 10 January at 2044 local time. There is no stable surface layer, and the profile is well mixed to 0.85 MPa. The N is less than 0.002 s^{-1} throughout the top 0.85 MPa and increases to about 0.01 s^{-1} below. Several sections of the mixed layer are gravitationally unstable, having negative N^2 (and falling in quadrant 4 of the gradient T–S diagram). The behavior below the top of the seasonal thermocline in the two cases is similar.

One complete diurnal cycle from 7 and 8 January is illustrated by the potential temperature (θ) profiles in Fig. 4. A portion of the J_b^0 time series is also plotted and the superimposed numbers correspond to the profile numbers; the positive values of J_b^0 (favorable to convection) are shaded. This sequence of profiles is not strictly a time series since the AMP drops were not all made in the same location or the same parcel of water.

Profile 1 was made at 2053 local time, four hours after sunset. Between 0 and 0.55 MPa, the mean potential temperature gradient, $\overline{\theta_z}$, was slightly negative and there were many small inversions suggesting over turning water parcels. Below 0.55 MPa, $\overline{\theta_z}$ was positive and there was less small-scale temperature structure. These observations suggest that the water column was

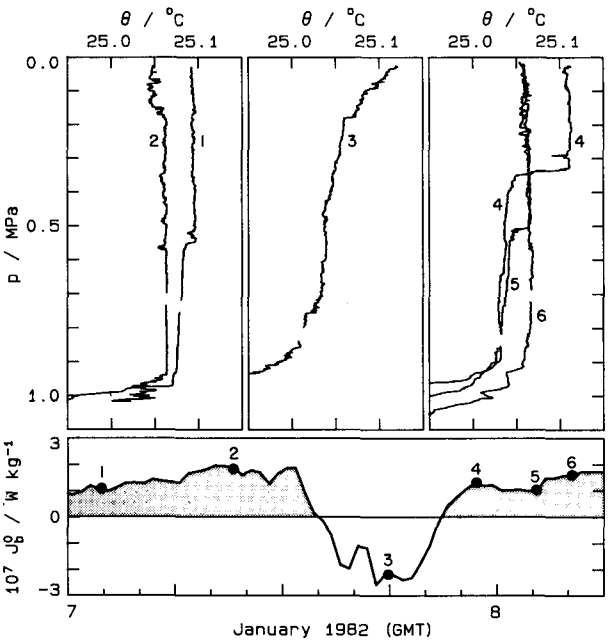

FIG. 4. The diurnal cycle from 7 to 8 January. The numbers near the large dots on the J_b^0 time series give the times of the corresponding θ profiles. Profiles 1 and 2 show the progressive penetration of the well-mixed layer down from the surface. Profile 3 shows the effects of daytime restratification. Profiles 4 through 6 show the erosion of the stratification during the next night. Because of lateral variability in θ and s and changes in ship position of a few km, the profiles are not a time series in one water parcel.

rapidly mixing above 0.55 MPa and not mixing below; the stable stratification below 0.55 MPa was the result of the absorption of solar radiation during the previous morning and afternoon.

Profile 2 was made 3.5 hours later. By that time, $\overline{\theta_z}$ was slightly negative and the water column was apparently rapidly mixing to nearly 0.95 MPa. Since temperature is a good indicator of density in this dataset, the temperature inversion in the upper 15 m of this profile is also an unstable density inversion.

Profile 3 is the only one of this sequence that was made during the daytime heating phase (1300 local time). The upper 15 m had been warmed and stabilized for several hours, and $\overline{\theta_z}$ was positive throughout the water column. The stable stratification below the surface layer was probably the result of a combination of solar radiation absorption and lateral intrusions. No drops were made later in the afternoon, so we do not know how warm the surface layer became.

Profiles 4–6 show the development of the convective mixed layer as the night progressed. The interpretation of these profiles is similar to that of profiles 1 and 2. As the mixing proceeded down from the surface, the stratification was destroyed and $\overline{\theta_z}$ became negative. The magnitude of the temperature step across the base of the mixing layer gradually decreased until the new mixing layer reached the seasonal thermocline near 1.0 MPa.

In the next section, the temperature observations are related to direct measurements of ϵ, and it will be shown that small temperature steps such as those at 0.35 and 0.50 MPa in profiles 4 and 5, respectively, correspond to the base of the mixing layer.

d. *Behavior of* ϵ

The mixing implied by the changes in the temperature profiles in Fig. 4 is confirmed by the direct measurements of ϵ. Figure 5 shows the ϵ profiles from the same six drops. The dissipation rate is very high ($\epsilon \gg 10^{-7}$ W kg^{-1}) between the surface and a pressure of 0.05 to 0.10 MPa; we call the corresponding depth L_s. These high dissipation rates are caused by direct wind forcing, surface wave breaking and vehicle motion. We have been unable to assess the relative contribution of each, and the region $L_s < z < 0$ will not be considered in what follows.

When conditions are favorable for convective mixing, i.e., when $J_b^0 > 0$, the ϵ profile was often nearly uniform with depth between L_s and a depth at which a decrease in ϵ of 1 to 3 orders of magnitude occurred. This depth is the effective mixed layer depth, D.

The diurnal mixed layer is a rapidly evolving system, and profiles were made at various stages. Profiles 1, 4 and 5 were made when convective mixing was penetrating down from the surface and remixing water that had become slightly restratified the previous afternoon. In these profiles, D is limited by small density steps

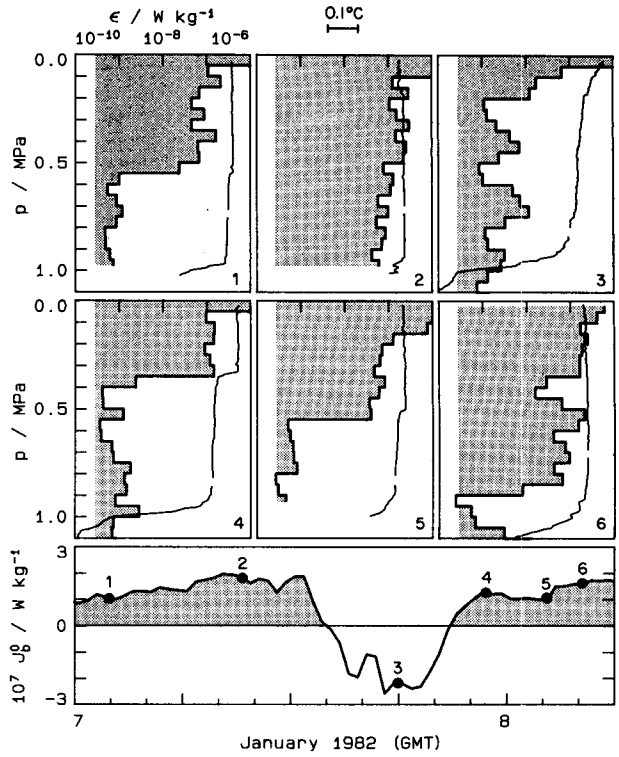

FIG. 5. The profiles of viscous dissipation rate, ϵ, corresponding to the θ profiles in Fig. 4. (θ is replotted in this figure for reference.) During the nighttime deepening periods, ϵ is nearly uniform until a large (1–3 orders of magnitude) decrease at the base of the mixing layer. The cutoffs occur near the same depths as do small θ steps. The high ϵ zone is smeared across the mixed layer base by the 5 m vertical averaging and by overturns at the base of the mixed layer (see Fig. 6). Above the steps the profiles are adiabatic, while below they are stably stratified. These small θ steps represent the effective depth of the mixed layer. At night, the mean value of ϵ in the mixed layer is close to J_b^0.

(and by the small potential temperature steps in Fig. 2); the depth of the seasonal thermocline was not relevant. Profiles 2 and 6 were taken in fully-developed convective mixed layers. In these cases, D corresponded to the depth of the top of the seasonal thermocline. In these five profiles, the mean value of ϵ in the depth range $L_s < z < D$ is (1.0 to 3.0) $\times 10^{-7}$ W kg^{-1}, close to J_b^0.

In daytime drops such as profile 3, the stable density gradient extends to the sea surface. The corresponding ϵ profile generally decreases rapidly below the surface and remains low in the restratified mixed layer ($\epsilon \ll 1.0 \times 10^{-8}$ W kg^{-1}). The energy provided by the wind stress was not enough to overcome the stabilizing effect of the incoming solar radiation and was quickly dissipated in the upper 20 m. Intermittent patches of higher ϵ in the restratifying surface layer (e.g., at 0.40 and 0.70 MPa in profile 3) were presumably caused by shear instability.

The correspondence between the depth of mixing and the change in temperature gradient is shown more

clearly in the expanded-scale plots in Fig. 6. Although the temperature profiles in the mixing layers appear to be superadiabatic, the pressure effect discussed in section 2 [(−3 to −9) × 10^{-5} °C m^{-1}] could account for most of the apparent gradient, and the profiles are probably nearly adiabatic. In these cases, the sharp cutoff in the ϵ profiles occurs within a meter of the transition from an adiabatic to stratified temperature profile. The temperature steps across the base of the mixing layers are less than 0.02°C; the corresponding density steps are less than 0.005 kg m^{-3}.

e. Velocity field

The major shear feature is associated with the intrusive finestructure between 1.2 and 1.5 MPa (Figs. 2 and 3). An XCP profile made about 40 minutes before the final AMP profile in Fig. 4 shows a decrease in vertical shear in the upper 0.30 MPa, small shear (less than 0.005 s^{-1}) below that, and an abrupt increase to a maximum of 0.02 s^{-1} between 1.2 and 1.5 MPa (Fig. 7). The mean velocity in the upper 1.2 MPa is between 0.10 and 0.20 m s^{-1} toward the south. This profile is typical of other XCP profiles made during the nighttime convective deepening of the mixed layer.

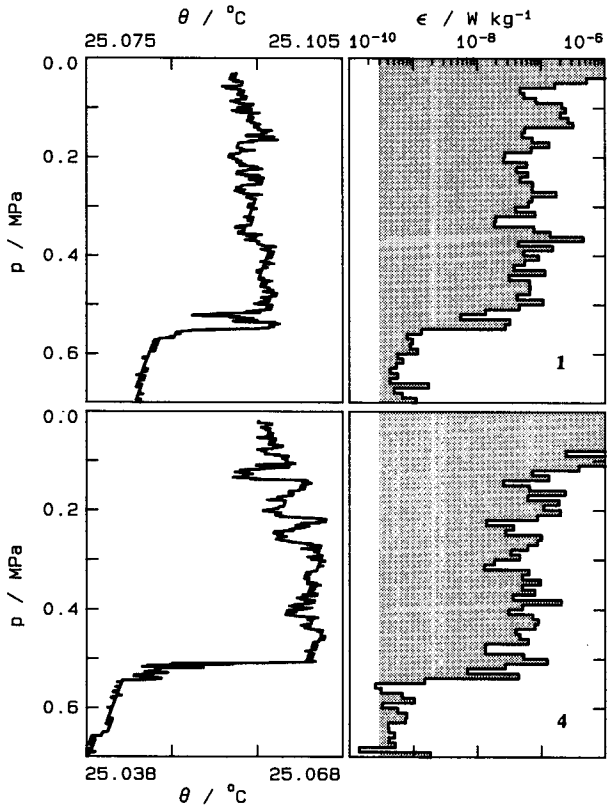

FIG. 6. Expanded scale plots of profiles 1 and 4 (Fig. 5) showing the correspondence between the θ and ϵ profiles during convective mixing. Note that the range of the θ scale is only 0.03°C. θ is averaged over 0.1 m in the vertical and ϵ is estimated in 1 m blocks. The mean values of θ_z in the mixed layers of profiles 1 and 4 are -7.1×10^{-5} °C m^{-1} and -11×10^{-5} °C m^{-1}, respectively. These values are about half the adiabatic temperature gradient at these s, T and p. Since this is close to the estimated pressure-induced error of these thermistors (J. Carlson, personal communication, 1985), the profiles are nearly adiabatic in the mixed layers. The depth of mixing, D, is clearly shown by the transition from an adiabatic to a stratified profile. The temperature steps at the base of the mixed layers are only 0.014 and 0.020°C in these two examples.

f. Summary

Data were taken during several cycles of a diurnal convective mixed layer. During the day, vigorous mixing was restricted to the upper 10–15 m of the water column since insolation was strong and winds were weak. At night, the surface stability zone eroded and convective mixing penetrated through the underlying slightly restratified surface layer. As the mixing proceeded, the mixed layer depth was distinguishable as the point at which the superadiabatic profile became subadiabatic. This was confirmed with direct dissipation measurements showing that ϵ undergoes a rapid decrease starting at this depth. The temperature steps defining the mixed layer base in these cases would often not be resolvable with instruments such as XBTs. During the nighttime convective periods, ϵ decreased gradually with depth within the mixed layer, and the mean values were near 1.0×10^{-7} W kg^{-1}, of the same order as J_b^0.

4. The warm-core ring

a. Background

In the upper ocean, convection is most likely to occur where warm surface water is exposed to cold air; a warm-core Gulf Stream ring is an ideal setting. Our measurements were made in warm-core ring 82-I in January 1983 (Larson and Gregg, 1983; Shay and Gregg, 1984a,b; Joyce and Stalcup, 1985; Kunze, 1986). In this region of the North Atlantic (41°N, 66°W), cold air outbreaks are common in the winter, and the large air–sea temperature contrast in warm-core rings enhances the surface heat loss. Thus, the turbulence measurements were made in the ring not to investigate ring dynamics, but to maximize the chance of observing convectively driven turbulence.

The structure and dynamics of the marine atmospheric boundary layer during cold air outbreaks have been investigated over the past decade. While cold air is advected over cold land, it does not gain a significant amount of heat from below. The transfer of sensible and latent heat from the ocean, however, results in convection and the growth of a mixed layer in the lower atmosphere. The initiation of convection is marked by the edge of a cumulus cloud band, preceded by a clear air band parallel to the coast (Chou and Atlas, 1982; Atlas et al., 1983).

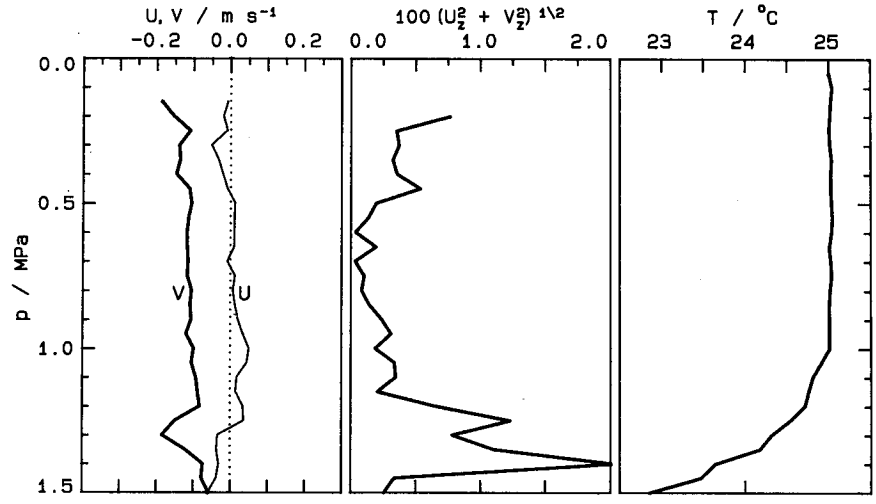

FIG. 7. Profiles of velocity (U, V), shear magnitude and temperature from an XCP drop made at 0330 GMT 8 January 1982. The temperature profile appears well mixed to 1.0 MPa and there is a shear maximum between 1.2 and 1.4 MPa. The closest AMP profile was made 20 minutes later and indicates that the mixing layer extends only to 0.70 MPa, near the depth of the shear minimum in this plot.

During two weeks of operations in ring 82-I, two cold air outbreaks were observed. The second (on 17 January) was the more severe and forced convective deepening of the mixed layer. The satellite photograph of the region above the ring on 19 January (Fig. 8, kindly provided by David Atlas) is typical of those taken during cold air outbreaks. The alignment of the cloud streets in the direction of the mean wind, the clear air band parallel to the coast, and the thickening of the cumulus clouds offshore are all characteristic of cold air outbreaks.

Warm-core ring 82-I was a small ring with a radius of about 40 km. In the two weeks between two XBT surveys (Joyce and Stalcup, 1985), the ring moved 90 km to the west-southwest following the 2000 m isobath. The surface of the ring was partially flooded by cold slope water before the first survey and its surface expression was obscured. During the second survey, the surface signal was more pronounced, with temperatures as much as 8°C higher than the surrounding slope water. The basic thermal structure and heat balance of the ring are discussed by Joyce and Stalcup (1985). Based on their two XBT surveys, they conclude that an outward lateral heat flux is needed to close the ring's heat budget and speculate that the flux occurred in a 50 m thick surface layer. Unfortunately, direct measurements are not available to test the hypothesis.

The large-scale velocity structure and internal wave field of the ring are discussed by Kunze (1986) and will only be summarized here. The azimuthal velocity maximum (about 0.50 m s^{-1}) occurs at a radius of about 35 km and a depth of about 100 m. Inside 25 km and above 300 m, the ring was in solid body rotation. The radial momentum balance was cyclogeostrophic to lowest order. When the asymmetry of the ring is taken into account, there is no net radial flow.

The operational objective of the turbulence experiment was to stay close to ring center, where conditions were expected to be more uniform than near the edges, and make frequent AMP profiles during a cold air outbreak. The positions of AMP bursts are shown in Fig. 9. The contours are the depth of the 7°C isotherm determined from the combined XCP and XBT datasets, and all data have been projected to a common ring center using the ring's mean translation speed. Bursts 26–35 were made on 19 and 20 January during the second cold air outbreak and are all within 20 km of ring center. Within a burst, the drops fell along a smooth track determined by the ship's wind drift. The separation between consecutive drops was 200 to 600 m.

b. Meteorological forcing

The weather was cold and windy during the ring experiment. Two storms passed through the area; a weak cold air outbreak followed the first storm and a severe cold air outbreak followed the second. The meteorological measurements are summarized in Fig. 10. Since we are mainly concerned with conditions near ring center, we have interpolated across two periods when we were sampling near the edge of the ring.

The wind forcing was much stronger in the ring than it was in the Bahamas. Peaks occurred during the two storms on 13 and 17 January. The maximum values of E_{10}, 10.0 and 13.0 W m^{-2} (corresponding to wind speeds of 18 and 20 m s^{-1}), were a factor of 10 higher than the maximum values in the Bahamas. Large sur-

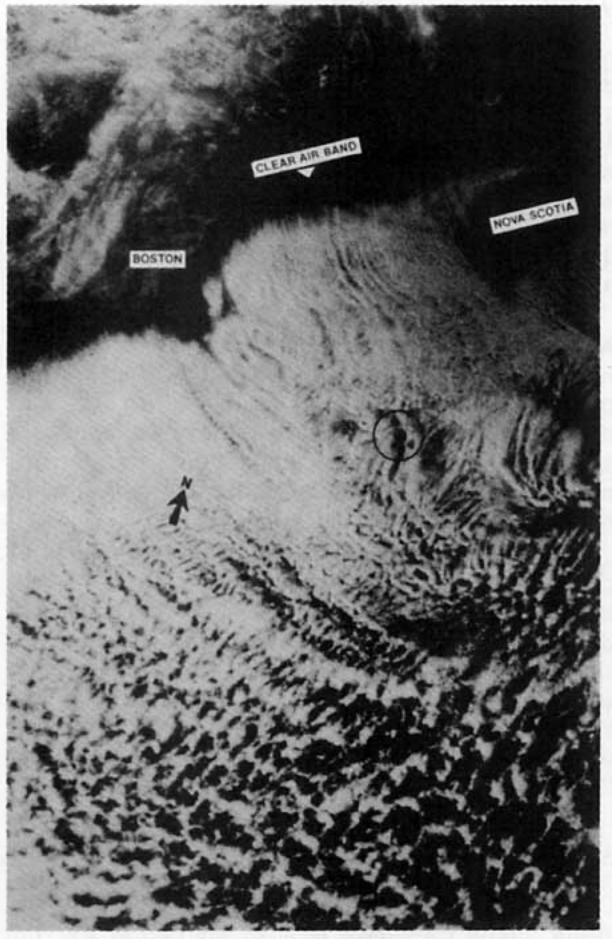

FIG. 8. A satellite image of the area around warm-core ring 82-I at 1840 GMT 19 January 1983. The circle marks the nominal position of the ring. The clear air band between the coast and the edge of the clouds is characteristic of cold air outbreaks. Where the transfer of heat from the ocean to the atmosphere is strong enough, a convective mixed layer grows in the atmosphere and cumulus clouds form. The orientation of the cloud streets shows the direction of the mean flow of cold air from the continent. (The photograph was provided by David Atlas.)

face waves accompanied the strong winds, making working conditions difficult.

During the first storm, J_q^0 reached a maximum of 500 W m^{-2}, and J_q^e/J_q^s was 2.6. The corresponding J_b^0 was 2.8 $\times$ 10^{-7} W kg^{-1}. A moderate cold air outbreak followed the storm and the air–sea temperature contrast reached 5°C.

The maximum heat loss during the second storm was higher; J_q^0 reached 600 W m^{-2}, and J_q^e/J_q^s was 3.4. The maximum value of J_b^0 was also higher, 3.2 $\times$ 10^{-7} W kg^{-1}.

During the cold air outbreak after the second storm, the wind forcing decreased by more than a factor of 5 ($E_{10} \approx$ 2.0 W m^{-2}, which matches the maximum values in the Bahamas), but J_q^0 and J_b^0 remained high because of the 13°C air–sea temperature difference.

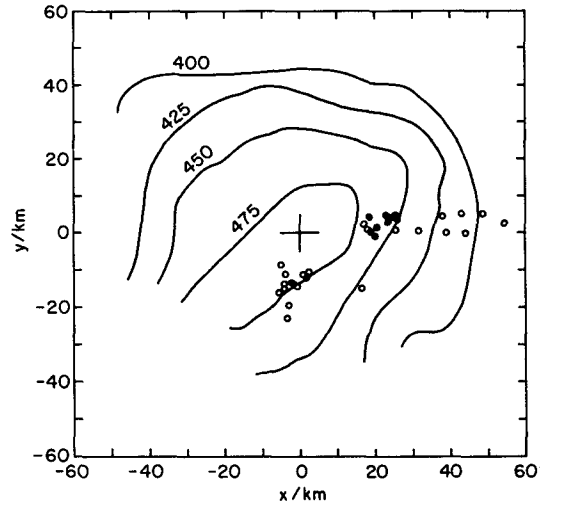

FIG. 9. The positions of AMP bursts projected to ring-center coordinates. AMP Bursts 26–35 (solid circles) were made during the cold air outbreak on 19–20 January. The contours are the depths of the 7°C isotherm. The temperature contours for this figure were provided by Eric Kunze, and are based on data from XCPs and the XBTs of Joyce and Stalcup (1985).

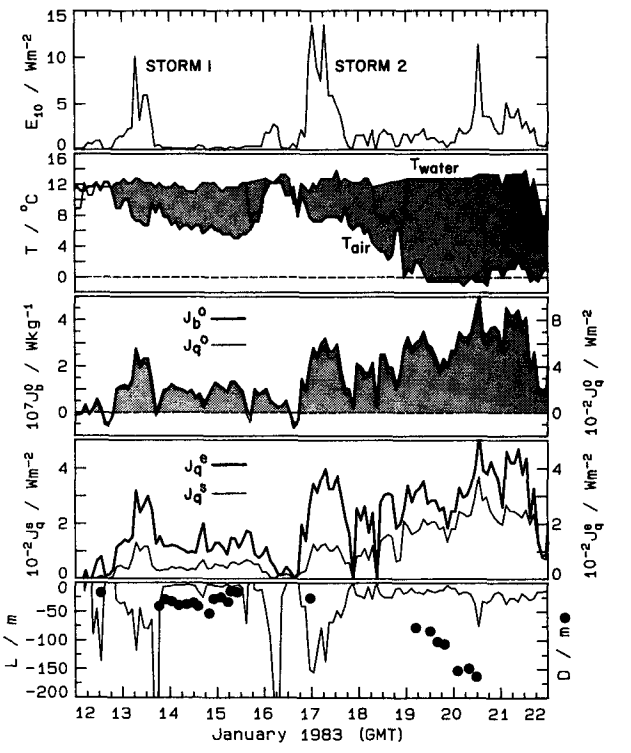

FIG. 10. Meteorological time series from the ring experiment, using data recorded every two hours in the ship's weather log. On 15 and 18 January, T_{water} decreased by several degrees (dashed lines) when we made measurements near the ring edge; fluxes were calculated by interpolating across these periods in order to reflect conditions near ring center. After Storm 2 on 17 January, a severe cold air outbreak forced convective deepening of the ring's mixed layer (solid circles in bottom panel). Maximum values of E_{10} are a factor of 10 higher and the contribution of J_q^s to J_q^0 is much greater than in the Bahamas. (Note that the scales are different from those in Fig. 1.)

Continuous AMP operations were run on 19 and 20 January when the average values of J_q^0 and J_b^0 were 620 W m^{-2} and 3.5×10^{-7} W kg^{-1}, respectively. The surface cooling was often made obvious by sea smoke, when visibility was not obscured by snow.

The mixed layer reached a maximum depth of 50 to 60 m following the first storm (● Fig. 10), but did not continue to deepen during the weak winds between storms. We were unable to make AMP drops during the second storm and did not make measurements in the ring center again until early on 19 January. By that time, D was 70 m, and increased to more than 150 m when operations stopped on 20 January. Although L was greater than in the Bahamas (because the wind forcing in the ring was stronger), D was also greater. Therefore, D/L was between 5 and 12, again weakly to moderately convective by atmospheric standards.

c. *Structure and evolution of the hydrographic field*

Within the core of the ring, the hydrographic field is characterized by a salt-stabilized temperature inversion in the upper 2.0 MPa; both θ and s reach maxima near 2.0 MPa. Before the arrival of the storms and cold air outbreaks, the upper 0.1 to 0.2 MPa contained a cap of cool (θ = 12.0°C), fresh (s = 0.0342) water, apparently a result of partial flooding of the ring surface by slope water (Joyce and Stalcup, 1985). AMP Burst 1 (Fig. 11a) is an example of the mean hydrographic profiles before the first storm. Below the surface cap (i.e., between 0.15 and 0.35 MPa), θ increases by 2.0°C and $10^3 s$ increases by 1.0; below this, the temperature and salinity gradients begin to decrease. Near 1.5 MPa, the gradients again increase until reaching the θs maximum. In the upper 0.5 MPa, N decreases steadily from a maximum of 0.014 s^{-1}. By 0.5 MPa, N is reduced to less than 0.002 s^{-1} and remains low until 1.5 MPa.

During the first storm, the mixed layer depth increased to 40 m, and the cool, fresh surface cap was partially eroded. In the calm period following the first storm, the mixed layer did not continue to deepen and we began a radial survey of the ring. While we were near the ring edge, the strong cold air outbreak began and we went back to the ring center to make AMP Burst 26 early on 19 January. The upper 0.7 MPa is now homogenized and the slope water cap is eroded (Fig. 11b). The maximum upper layer stability frequency is about 0.004 s^{-1} in a broad region from 0.7 to 1.2 MPa. The density change across the base of the mixed layer is only 0.05 kg m^{-3}.

The mixed layer continued to deepen under the influence of the cold air outbreak for the next two days. AMP Burst 33 was made early on 20 January; by then the mixed layer was more than 150 m deep. The density profile (Fig. 11c) shows that the upper 1.5 MPa are well mixed. There were strong lateral gradients and intermittence present in the ring even during the intense convective mixing forced by the cold air outbreak.

d. *Behavior of* ϵ

Accompanying the hydrographic changes was an evolution of the turbulence field similar to that during a night in the Bahamas. Before the first storm (Fig. 12a), ϵ is high near the surface ($\epsilon > 10^{-6}$ W kg^{-1}), but rapidly drops to 4×10^{-10} W kg^{-1} at 0.5 MPa. This burst was made when surface cooling was small ($J_q^0 \approx 0$) because of the small air–sea temperature contrast. The mixing in the upper 0.35 MPa is predominantly wind-driven.

By AMP Burst 26, the convective mixed layer was well established (Fig. 12b). Below the wave zone, ϵ falls to a mixed layer value of $\bar{\epsilon} = 2.5 \times 10^{-7}$ W kg^{-1}, comparable to $J_b^0 = 3 \times 10^{-7}$ W kg^{-1}. The ϵ then decreases by two orders of magnitude across the mixed layer base and intermittently rises in patches throughout the upper 2.5 MPa. This profile is similar to a typical night time ϵ profile from the Bahamas (Fig. 5).

One day later, the mixed layer is more than 150 m deep and ϵ is high throughout (Fig. 12c). The mean mixed layer value of ϵ is 2.7×10^{-7} W kg^{-1} and J_b^0 is 3.2×10^{-7} W kg^{-1}. Near the base of the mixed layer, the decrease of ϵ is only a factor of 10 since the mixed layer has now penetrated into a zone of elevated dissipation, which has been attributed to the combined effects of shear and double diffusion by Larson and Gregg (1983).

e. *Velocity field*

The large-scale shear field changed little during the deepening of the mixed layer in the part of the ring observed during the cold air outbreak. XCP 1169 (Fig. 13a) was made immediately upon our arrival back near ring center after the beginning of the cold air outbreak. The flow in the upper 1.6 MPa is predominantly southward and the mean speed decreases from 0.45 m s^{-1} at 0.30 MPa to 0.30 m s^{-1} at 1.6 MPa. After an initial decrease in the upper 0.5 MPa, the vertical shear remains low (less than 0.005 s^{-1}) before increasing to more than 0.01 s^{-1} in the intrusion below 1.5 MPa. The XCP profile indicates a mixed layer base between 0.6 and 0.7 MPa.

XCP 1171 (Fig. 13b) was made about 28 hours after XCP 1169. The mixed layer has deepened to about 1.5 MPa, but the velocity is still predominantly toward the south (although changes in the vertical are somewhat smaller) and the shear profile is about the same as earlier. The maximum shear is still in the intrusion below 1.5 MPa, but now that depth closely corresponds to the mixed layer depth.

f. *Summary*

Warm core ring 82-I was a small ring, with a radius of about 40 km. The azimuthal velocity maximum was at a radius of 35 km and a depth of 100 m. Before the first of two storms, the ring surface was partially capped

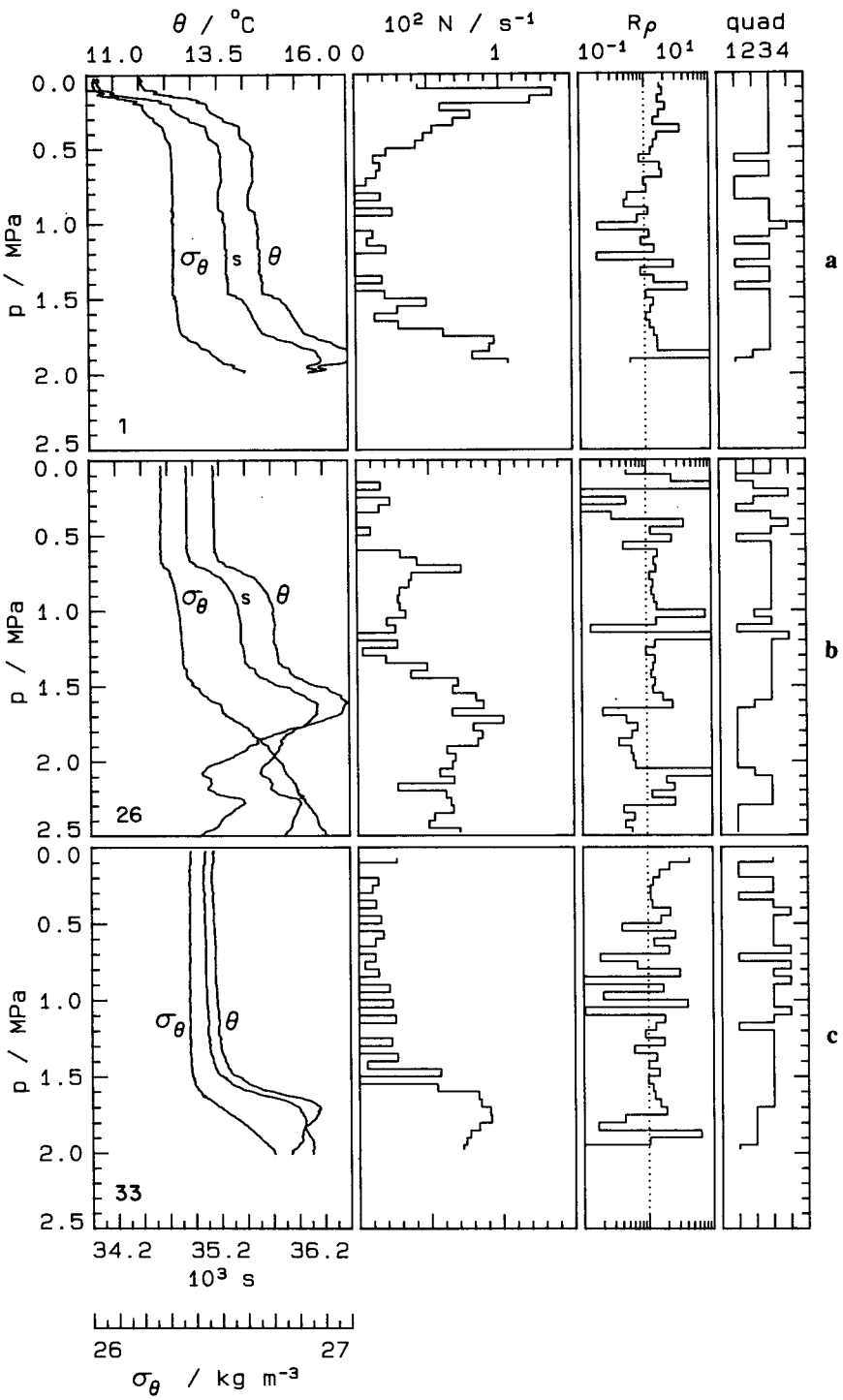

FIG. 11. Evolution of the hydrographic profiles near ring center. Each profile is an average of 2–6 drops in an AMP burst; all drops in the burst-averages extended to the same depth. The s, θ and σ_θ profiles are 0.5 m vertical averages (burst numbers in lower left). N, R_ρ and quad are estimated in 5 m blocks. (a) AMP Burst 1 (1530 GMT 12 January 1983), the initial condition before the cold air outbreak; the ring is capped by cool, fresh water. (b) AMP Burst 26 (0330 GMT 19 January 1983), made during the cold air outbreak following the second storm. The mixed layer now extends to 0.70 MPa. (c) AMP Burst 33 (0400 GMT 20 January 1983), made one day after Burst 26. Now the mixed layer extends to more than 1.5 MPa.

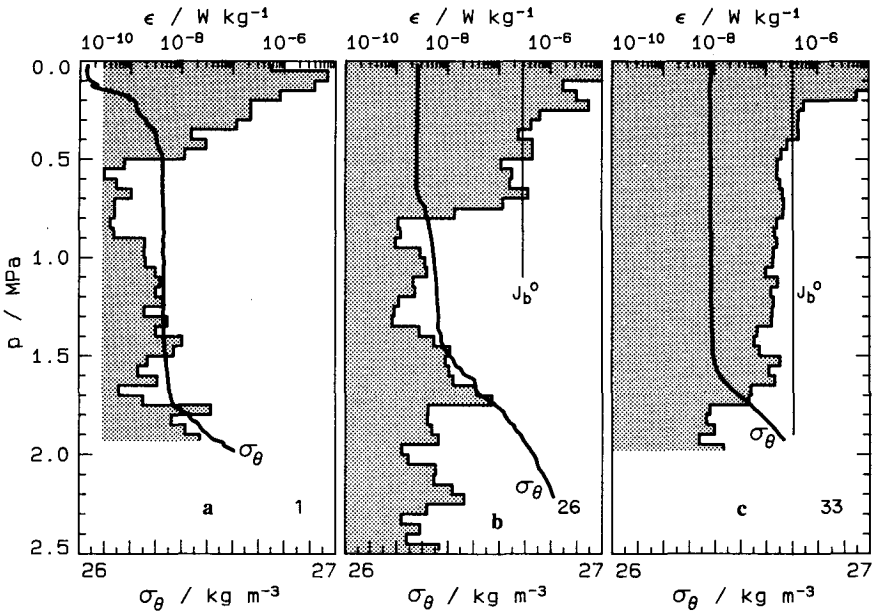

FIG. 12. Profiles of ϵ corresponding to the hydrographic profiles in Fig. 11 (σ_θ is replotted in this figure for reference; burst numbers in lower right). The burst-averages are averaged in 5 m blocks. J_b^0 is indicated by the vertical lines in panels b and c. Before the first storm (a), ϵ decreases steadily from the surface. The profiles made during the cold air outbreak (b and c) are similar to those made at night in the Bahamas (see Fig. 5).

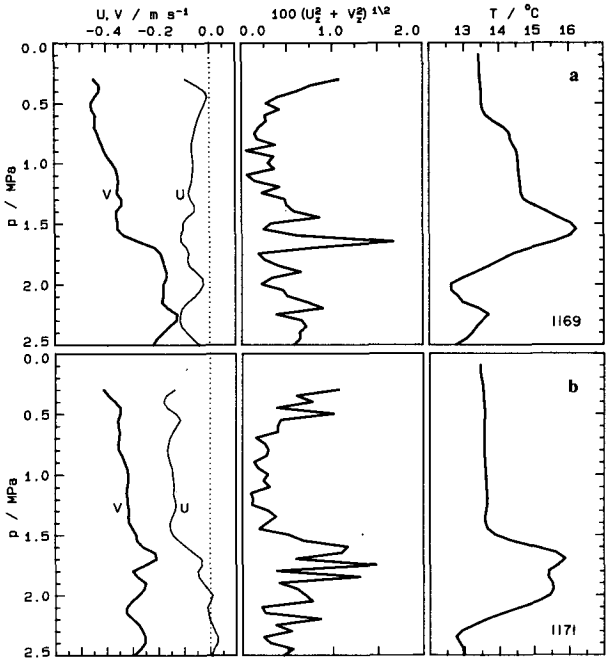

FIG. 13. Profiles of velocity (U, V), shear magnitude and temperature from two XCP drops made during the cold air outbreak (drop numbers in lower right). (a) XCP 1169 made on 19 January 1983 at 0150 GMT (just before AMP burst in Fig. 11b). The flow is predominantly to the south and the shear decreases rapidly in the upper 0.50 MPa before again increasing in the intrusion at 1.6 MPa. The mixed layer extends to about 0.65 MPa. (b) XCP 1171 made on 20 January 1983 at 0530 GMT (an hour before the AMP burst in Fig. 11c). The velocity and shear fields are similar to those from XCP 1169, but the mixed layer has deepened to nearly 1.5 MPa.

by cool, fresh slope water. The first storm homogenized the upper 0.35 MPa and partially eroded the slope-water cap. A severe cold air outbreak followed the second storm. During the cold air outbreak, the mixed layer deepened to more than 150 m, driven by convection forced by the rapid surface cooling. The mean value of ϵ during the convectively driven deepening, $\sim 3.0 \times 10^{-7}$ W kg^{-1}, was of the same order as the surface buoyancy flux and decreased gradually through the mixed layer. Near the end of the measurements, the mixed layer had deepened into a region containing a horizontal intrusion and shear maximum. Even during the intense mixing phase, there was a large amount of lateral variability in both hydrographic and turbulence fields.

5. Dissipation rates in the mixed layers

In this section, we discuss the behavior of ϵ in the mixed layers during the convective periods of both experiments; i.e., during the night in the Bahamas and during the second cold air outbreak in the ring. First, we discuss the probability distributions of the dissipation data to assess the validity of our estimates of the mean values. Second, we show that there is significant variability of ϵ profiles between drops in a single burst. Finally, using convective mixed layer scaling, we compare the results with data from the atmospheric mixed layer.

We have selected profiles made when convection was the dominant process. Thus, drops made when

there is evidence of either significant horizontal advection (revealed by intrusions) or large horizontal gradients are not used. About 70 nighttime drops from the Bahamas (made on each of several days) and 45 drops from the second cold air outbreak in the ring are used.

a. *Probability distributions*

An approximately lognormal probability distribution is expected for small-scale gradient quantities, such as dissipation rates, in fully developed, homogeneous, isotropic turbulence (Gurvich and Yaglom, 1967). More important for the experimentalist, the accuracy of statistics such as $\bar{\epsilon}$ depends on the characteristics of the distributions (Washburn and Gibson, 1984). If the tails of the distribution are undersampled, then mean values will be poorly estimated. Several authors have investigated the statistics of ϵ or χ in the thermocline, where the distribution functions are nearly lognormal over at least a small portion of the ranges of ϵ and χ (Gregg et al., 1973; Osborn, 1978; Elliott and Oakey, 1980). The average dissipation rates in the thermocline are so low, however, that the distributions are distorted owing to the accumulation of values near the instrumental noise levels (Washburn and Gibson, 1984; Moum and Lueck, 1985; Gregg et al., 1986). In an active convective mixed layer, the dissipation rates are high enough that the instrumental noise level should not affect the distribution; some distortion of the distribution will result from the underestimate of high values of ϵ caused by early termination of the integration (see the Appendix).

The probability density functions (pdfs) and empirical–theoretical quantile–quantile (q–q) plots of all the 0.5 m estimates of $\log(\epsilon)$ in $D < z < L_s$ are shown in Fig. 14. The pdf of the Bahamas data (Fig. 14a) resembles a lognormal pdf more than does that of data from the thermocline (it is symmetrical about its mode and not skewed toward the instrumental noise level). The q–q plot is a generalized form of the familiar probability plot; empirical quantiles (the value of ϵ associated with a given cumulative probability) are plotted against theoretical quantiles (obtained by inverting the assumed theoretical distribution—in this case, a lognormal distribution); if the distributions are identical, then the points lie along a line with slope = 1 (Chambers et al., 1983). The distribution passes the test for lognormality at the 95% confidence level throughout the range of ϵ. [The small panels above the pdf and q–q plot show where the data are within ($C = 1$) or outside ($C = 0$) the 95% confidence bands.]

The pdf of the ring data (Fig. 14b) also is more lognormal than pdfs from the thermocline, although the peak is offset to the right. Because of this offset, the q–q plot shows that the distribution is not lognormal at the 95% confidence level; the test fails in the band $6 \times 10^{-8} < \epsilon < 1.4 \times 10^{-7}$ W kg^{-1} near the center of the pdf.

Given the resemblance of the pdf to lognormal pdf, there are several ways of estimating the mean value of ϵ (Washburn and Gibson, 1984; Baker and Gibson, 1986). The results are summarized in Table 1. The variance of $\ln(\epsilon)$ (σ^2) and maximum likelihood estimates (ϵ_{mle}) are found by linear fits to the high ϵ portion of the cumulative probability distributions (see Washburn and Gibson, 1984 and Gregg et al., 1986). The values of σ^2, 1.55 for the ring and 1.44 for Bahamas, are low compared with typical thermocline values (Baker and Gibson, 1986), and somewhat lower than those found by Osborn and Lueck (1985) for dissipation data acquired by a submarine in an actively mixing surface layer. The $\bar{\epsilon}$ and ϵ_{mle} agree to within 10%, and, in the rest of this paper, mean values of ϵ refer to arithmetic means.

b. *Variability of ϵ within bursts*

Before discussing the mean properties of ϵ profiles in the next section, it is necessary to point out that there is significant variability among the profiles in a single burst. Figure 15 shows a sequence of ϵ profiles made within a half-hour period near 0200 GMT 7 January 1982 (i.e., a Bahamas burst). The depth of the seasonal thermocline at this time was about 1.0 MPa, so this mixing was proceeding in weakly stratified water. The vertical resolution of these profiles is 0.5 m so that patches with small vertical scales and the sharpness of the cutoff of high ϵ at the mixed layer base are both obvious.

Even within the mixed layers, individual estimates of ϵ vary by more than a factor of 10. In drops 283 and 291, ϵ decreases steadily through the mixed layer while in the others the behavior appears more random. The depth of the mixing layer varies from 0.46 MPa in drop 283 to 0.56 MPa in drop 285 (taken 7 minutes later). The mean profile appears much more uniform within the mixed layer, having a gradual decrease of $\epsilon(p)$ followed by the sudden cutoff near the mixed layer base. This decrease, however is more diffuse in the mean profile than in any of the individual profiles because of the variability of the depth of the mixed layer.

Figure 16 is a similar sequence of drops from the ring. (The gaps in these profiles are sections that contain cable jerks.) The five drops span about 1 hour starting at 0200 GMT 19 January 1983. Like the profiles in Fig. 15, these have mixing patches with a variety of vertical scales. Despite the strong buoyancy forcing throughout the burst, $\bar{\epsilon}$ in the mixing layers of drops 1284 and 1285 is considerably less than in the other drops (although still significantly greater than $\bar{\epsilon}$ below the mixing layer). These two sequences of profiles illustrate the importance of making multiple drops even during periods of strong forcing.

c. *Convective mixed layer scaling*

It has been established in the atmospheric literature that a set of simple scaling laws is useful for describing

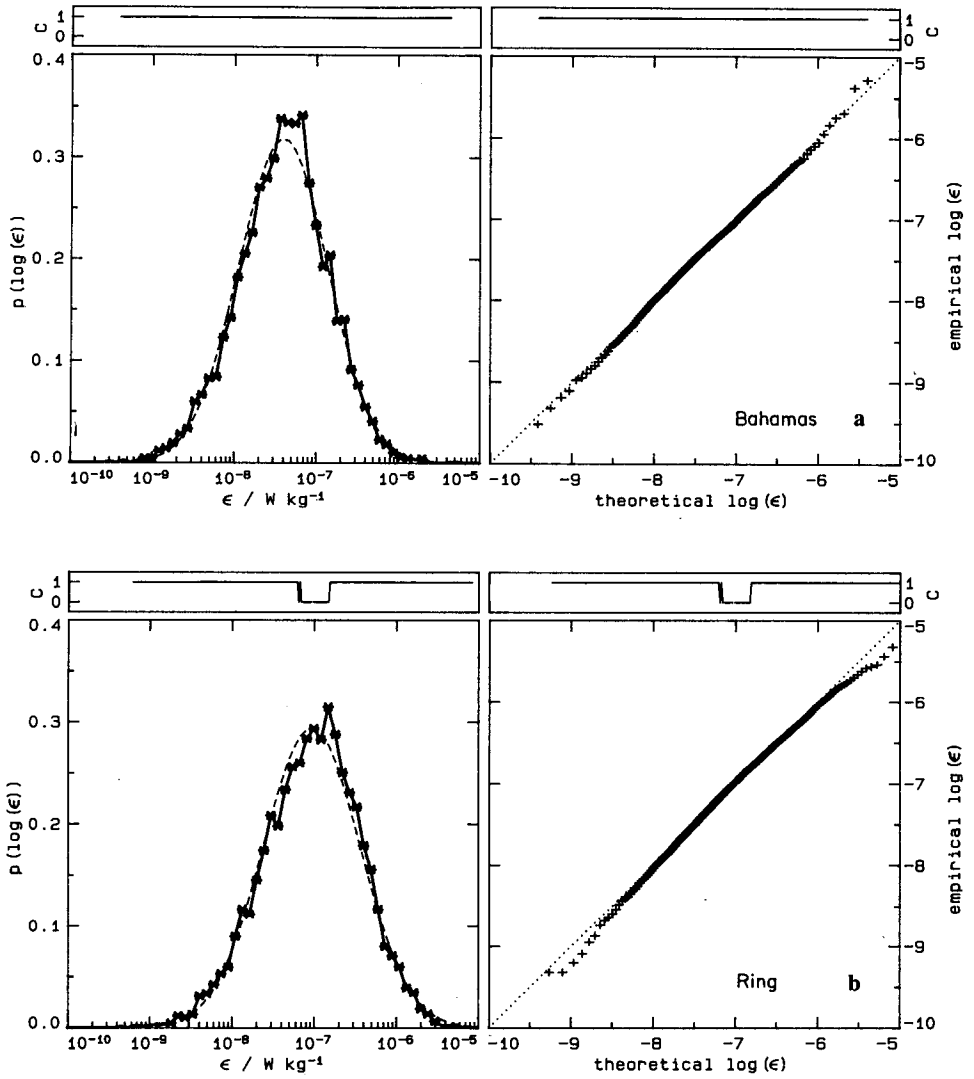

FIG. 14. Probability density function and empirical-theoretical q–q plot of the 0.5 m estimates of log(ϵ) from the mixed layers ($D < z < L_s$). The lognormal density with the same mean and variance as the data is plotted as a dashed line. If the data and theoretical distributions are the same, then the points in a q–q plot lie along a line with slope = 1. The function C in the small panels has a value of 1 when the distributions are the same at the 95% confidence level and 0 when they are not. (a) Bahamas. In this case, the data distribution is lognormal at the 95% confidence level. (b) Ring. This distribution fails the test for lognormality ($C = 0$ in top panels) at the 95% confidence level in the band $6.0 \times 10^{-8} < \epsilon < 1.4 \times 10^{-7}$ W kg^{-1}.

some properties of the turbulence in highly convective conditions ($D/L \gg 1$) when, far from the surface ($z/L > 1$), the surface shear stress can be considered unimportant. Under these conditions, the characteristic length, velocity, and time scales are

$$l_* = D \qquad [\text{m}] \tag{7}$$

$$W_* = (DJ_b^0)^{1/3} \qquad [\text{m s}^{-1}] \tag{8}$$

$$T_* = \frac{D}{W_*} \qquad [\text{s}]. \tag{9}$$

Terms in the turbulence balance equations, nondimensionalized using this set of scales, should be universal functions of the nondimensional depth

TABLE 1. Estimates of the mean value of ϵ in the mixed layers ($D < z < L_s$). $\bar{\epsilon}$ is the arithmetic mean, σ^2 is the variance of ln(ϵ) based on a linear fit to the cumulative probability distribution, and ϵ_{mle} is the maximum likelihood estimate for lognormal distributions.

	Ring	Bahamas
$\bar{\epsilon}$	2.14×10^{-7}	8.42×10^{-8}
σ^2	1.55	1.44
ϵ_{mle}	2.12×10^{-7}	7.82×10^{-8}

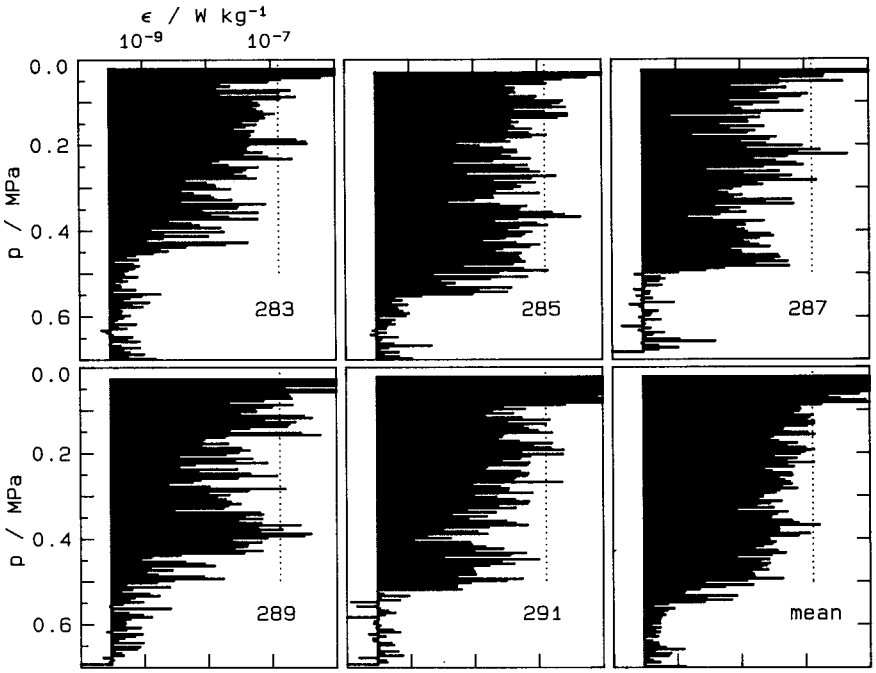

FIG. 15. Sequence of ϵ profiles from a single AMP burst in the Bahamas (0200 GMT 7 January 1982) spanning about 30 minutes. The vertical resolution is 0.5 m. The vertical dotted line is J_b^0 and the drop number is in the lower right of each panel. Even in this actively turbulent mixing layer there is a large amount of intermittence over small vertical scales. Note the sharpness of the cutoff of ϵ at the mixed layer base in several of the profiles. The final profile is the mean of the other five and is more uniform and has a more diffuse base.

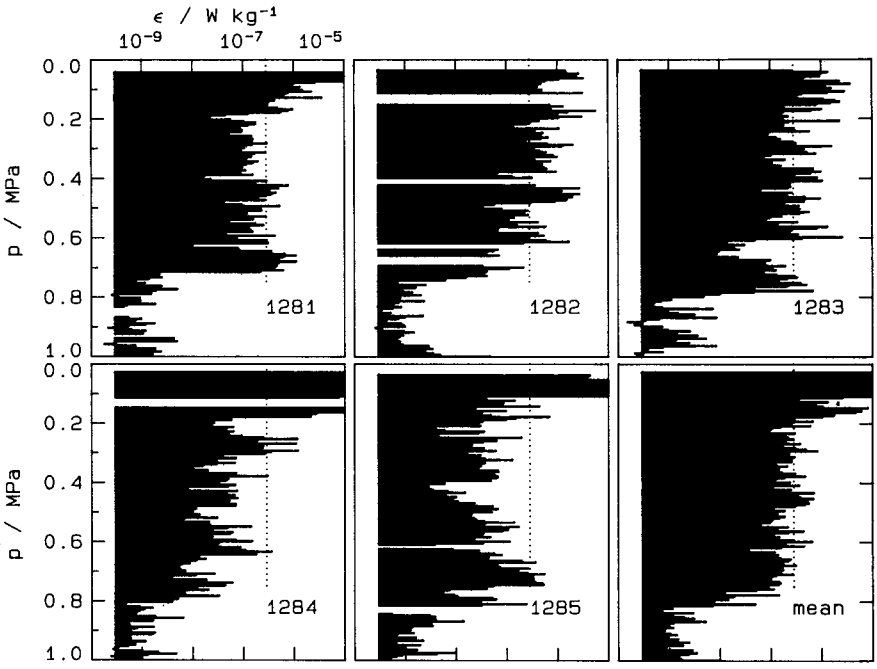

FIG. 16. Sequence of ϵ profiles from a single AMP burst in the ring (0200 GMT 19 January 1983) spanning about one hour. The vertical resolution is 0.5 m. The vertical dotted line is J_b^0 and the drop number is in the lower right of each panel. The $\bar{\epsilon}$ in the mixed layer of drops 1284 and 1285 is considerably smaller than in the other drops. (The gaps in these profiles result from editing of sections with cable jerks.)

$\delta = z/D$. This scaling works well for highly convective conditions over land (Kaimal et al., 1976; Caughey and Palmer, 1979; Guillemet et al., 1983), but less well when applied to the less convective marine atmospheric boundary layer (Nicholls and Readings, 1979), where changes with D/L are noted.

Using the convective mixed layer scales, the dimensionless form of the viscous dissipation rate becomes

$$\Psi = \frac{\epsilon D}{W_*^3} = \frac{\epsilon}{J_b^0}. \tag{10}$$

The selected drops are treated as an ensemble for convective mixed layer scaling. The dissipation data in $D < z < L_s$ from each profile are scaled using the local convective mixed-layer scales, averaged in bins of width $0.05D$, and then averaged across all profiles in the ensemble. [This procedure differs from that in Shay and Gregg (1984a,b) where the data in $D < z < L$ were used. Here L_s is used since the high dissipation surface zone often penetrates past L; L_s is generally within a factor of 2 of L.]

The results of applying convective mixed-layer scaling to ϵ from the two oceanic datasets and one dataset from the atmosphere are shown in Fig. 17. [The mean value in each δ bin and the 95% confidence intervals are shown. The confidence intervals are estimated using the bootstrap method (Efron and Gong, 1983).] The Ψ decreases gradually with depth (by no more than a factor of 3) in the mixed layer ($\delta < 1$) before starting a sudden decrease near the base of the mixed layer ($\delta \approx 1$). The mean values of Ψ within the mixed layer are 0.61 for the Bahamas data and 0.72 for the ring data.

The expected value for $\bar{\Psi}$ can be calculated if the TKE balance is between buoyant production and viscous dissipation, and the buoyant production rate is J_b^0 at the surface and decreases in a simple way through the mixed layer. For example, if the buoyant production decreases linearly to 0 at the base of the mixed layer [$J_b(z) = J_b^0(1 + z/D)$] then,

$$\frac{1}{D}\int_{-D}^{0} \epsilon(z)dz = \frac{1}{D}J_b^0 \int_{-D}^{0}\left(1+\frac{z}{D}\right)dz = \frac{1}{2}J_b^0 \quad [\mathrm{W\,kg^{-1}}]. \tag{11}$$

Here, a mixed layer value of $\bar{\Psi} \approx 0.5$ is expected; other forms of the buoyant production profile would lead to different expected values for $\bar{\Psi}$, but reasonable forms lead to $\bar{\Psi}$ of order 1. Thus, the oceanic values of $\bar{\Psi}$ in the mixed layer are close to the value expected for a convective mixed layer.

Results from experiments in the atmospheric boundary layer are also plotted in Fig. 17. The data are from the Minnesota Experiment (Kaimal et al., 1976) and the Aschurch Experiment (Caughey and Palmer, 1979). Each point represents the average of several time-averaged values of Ψ (the time averages were usually over 30 to 75 minutes). In the atmospheric experiments, dissipation is inferred from the inertial subrange of velocity spectra measured at fixed heights in the boundary layer. As the boundary layer evolves

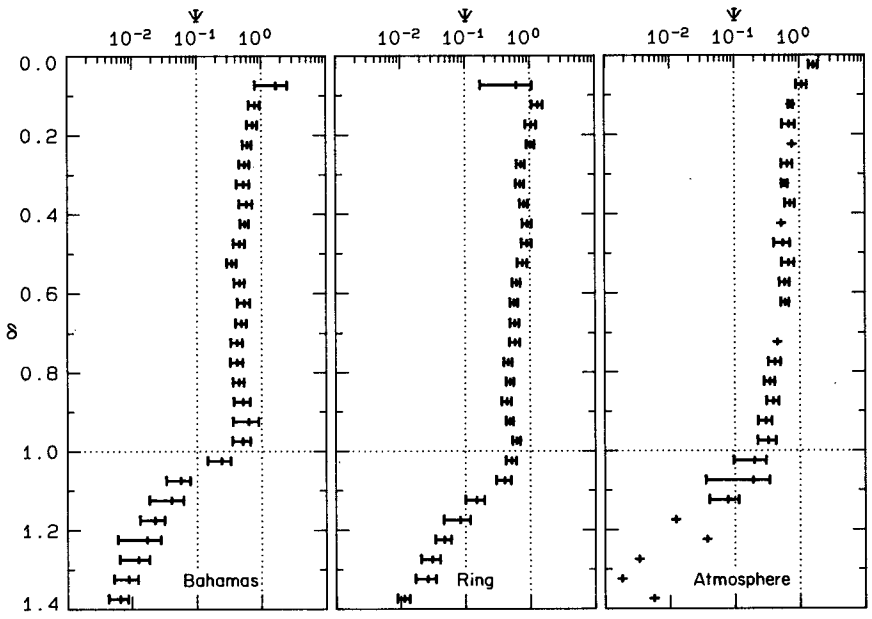

FIG. 17. Profiles of viscous dissipation rate nondimensionalized using convective mixed layer scaling. The atmospheric data are from Caughey and Palmer (1979) and have been ensemble averaged to appear on the same δ grid as the oceanic data. The error bars are 95% confidence intervals calculated using the bootstrap method. The mean values of Ψ in the mixed layers ($0 < \delta < 1$) are 0.61 (Bahamas), 0.72 (ring) and 0.64 (atmosphere).

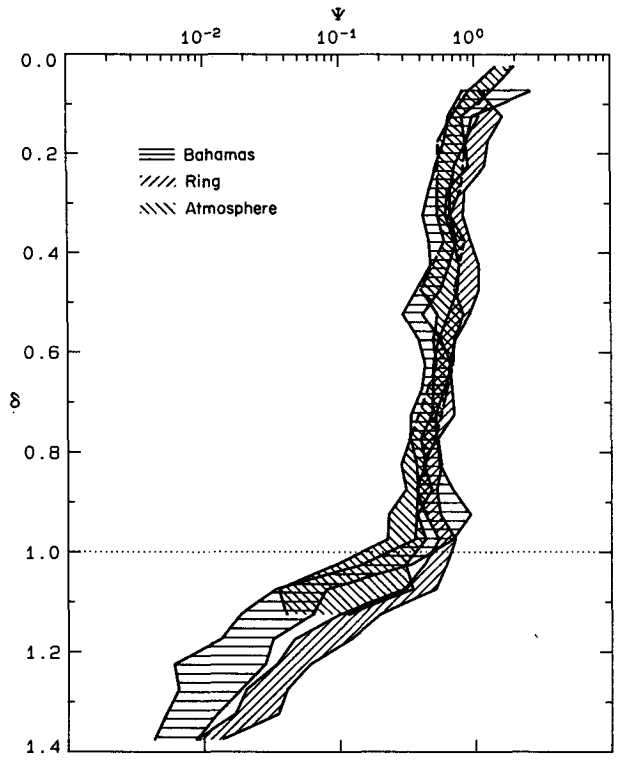

FIG. 18. Envelopes of the 95% confidence intervals overlaid to show that, at most depths in the mixed layer, the three datasets are statistically the same.

and deepens, D changes and a range of δ results. These data also produce a $\Psi(\delta)$ profile similar to the two oceanic profiles. The mean mixed layer value, $\bar{\Psi} = 0.64$, is between the two oceanic values. In an analysis of data from a reservoir, Imberger (1985) finds $\bar{\Psi} \approx 0.45$.

The confidence intervals show that the ranges of all three datasets overlap and that the mean values are statistically indistinguishable at the 95% confidence level through most of the mixed layer. This is seen more clearly in Fig. 18 where the envelopes of the 95% confidence intervals are overlaid. The three curves diverge only in the last 10% of the mixed layer, where the oceanic results are higher. This difference may be because shear across the mixed layer base is more important in the ocean. The atmospheric data were carefully edited to exclude profiles from periods of strong mixed layer shear (Caughey and Palmer, 1979), while no similar editing procedure was followed for the oceanic datasets.

No systematic effect of the bulk stability parameter D/L is found. In Figs. 19 and 20, the drops are grouped into ranges of D/L before being nondimensionalized; higher values of D/L imply that the conditions are more strongly convective. There are variations among the stability classes, but no systematic changes are seen. Nicholls and Readings (1979) and Deardorff (1972) find departures from typical mixed layer behavior for $D/L < 10$. The scatter in the oceanic profiles may be

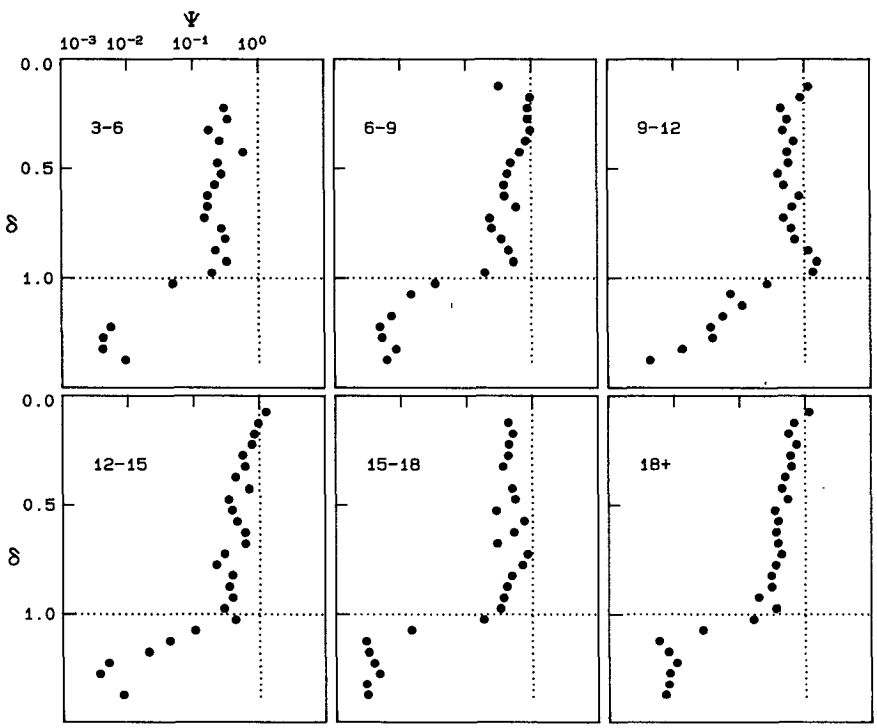

FIG. 19. Bahamas nondimensional viscous dissipation profiles grouped in stability classes. The numbers in the upper left of each panel give the range of the bulk stability parameter D/L; e.g., 3-6 means $3 < D/L < 6$. There is no systematic variation of Ψ with D/L.

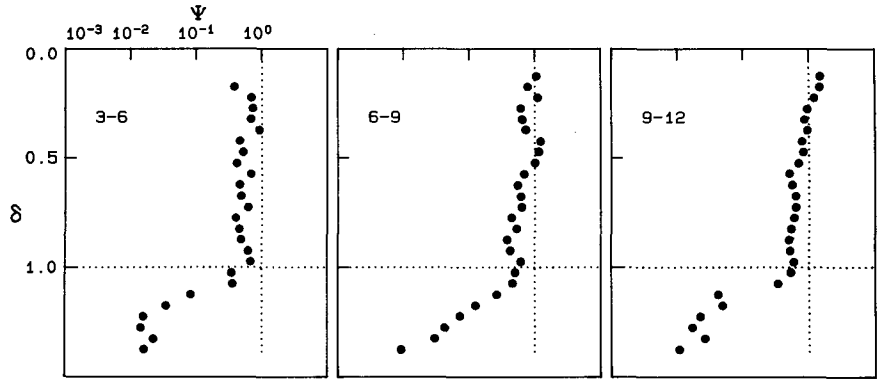

FIG. 20. Ring nondimensional viscous dissipation profiles grouped in stability classes. Again, there is no systematic variation of Ψ with D/L.

great enough to obscure similar results. In general, Ψ behaves as it does in the mean profiles. The lowest stability class ($3 < D/L < 6$) in the Bahamas (Fig. 19) is the only case that is atypical; $\bar{\Psi}$ is lower than in all other cases. The equivalent profile from the ring (Fig. 20) does not show a similar decrease of $\bar{\Psi}$.

The importance of this comparison of results is twofold. First, the agreement of the oceanic datasets shows that convective mixed layer scaling is a useful tool for describing the viscous dissipation rate in the oceanic convective mixed layer. Second, the agreement between the oceanic and atmospheric results extends the range of geophysical flows to which convective mixed layer scaling has been shown to apply; together, the oceanic and atmospheric boundary layers span a much wider range of conditions than does either alone.

6. Summary and discussion

Two experiments were performed to study the characteristics of turbulence in convective mixed layers in the ocean. In the first experiment, the mixed layer was forced by nighttime evaporative cooling and low winds. A diurnal cycle of mixed layer deepening at night and stabilization by absorption of solar radiation during the day was established. In the second experiment, the mixed layer of a Gulf Stream warm-core ring deepened from less than 50 m to more than 150 m in a little more than a day under the influence of surface cooling forced by a cold air outbreak and strong winds.

The major results are:

1) In both mixed layers, convective mixed layer scaling produces similar profiles of the rate of viscous dissipation of turbulent kinetic energy, ϵ.

2) The mean values of $\Psi = \epsilon/J_b^0$ from the two oceanic experiments and from atmospheric measurements are statistically the same throughout the bulk of the mixed layer ($D < z < L$).

3) There is no systematic effect of the variation of the stability parameter D/L, at least in the range ($3 < D/L < 76$) observed in the two experiments.

4) Although the results for ϵ are encouraging, the choice of D can be difficult. The base of the oceanic mixed layer often is not as obvious from hydrographic profiles as is the atmospheric inversion base from temperature soundings. In particular, if an instrument was unable to resolve temperature steps of 0.005 to 0.02°C, then D in the Bahamas dataset often would have been overestimated by a factor of 2 or more. This obviously makes comparison with the output of numerical models subject to error.

Given the comparison of results from the ocean and atmosphere, it is possible to assess the range of applicability of convective mixed layer scaling and the restrictions imposed by the assumptions. The two boundary layers span a wide range of conditions, and this can be illustrated by considering some of the bulk properties of the oceanic and atmospheric layers. Table 2 is based on $u_{10} = 10$ m s^{-1} and $J_q^0 = 500$ W m^{-2}, which were typical over the ring during the cold air outbreak.

TABLE 2. Comparison of the oceanic and atmospheric boundary layers. ρ, α and c_p are properties of the medium (air or seawater). J_q^0, u_*^3, J_b^0 and D are characteristics of the flow either directly measured or calculated from measured data. L, W_* and T_* [Eqs. (4), (8) and (9), respectively] result from dimensional analysis.

Property		Ocean	Atmosphere	Ocean / Atmosphere
ρ	[kg m^{-3}]	1025	1.25	820
α	[K^{-1}]	2.5×10^{-4}	3.5×10^{-3}	7.1×10^{-2}
c_p	[JK^{-1} kg^{-1}]	4.0×10^{3}	1.0×10^{3}	4.0
J_q^0	[W m^{-2}]	500	500	1.0
u_*^3	[m^3 s^{-3}]	2.0×10^{-6}	4.7×10^{-2}	4.2×10^{-5}
J_b^0	[W kg^{-1}]	3×10^{-7}	1.4×10^{-2}	2.2×10^{-5}
D	[m]	100–200	1000–2000	0.1
L	[m]	−17	−8.5	2.0
D/L	—	6–12	120–240	0.05
W_*	[m s^{-1}]	0.027–0.034	2.4–3.0	0.01
T_*	[s]	3700–5900	420–670	9

In the ocean, both μ_*^3 and J_b^0 are less than 10^{-4} of the corresponding values in the atmosphere. This is a consequence of the much higher density (ρ) and lower thermal expansion coefficient (α) of seawater compared with air. Since the mean stability of the stratified lower atmosphere is about the same as the ocean thermocline [the mean value of N in the troposphere is about 0.01 s^{-1} (Gill, 1982)], and the forcing in the ocean is so much weaker, ocean mixed layer depths, D, are much shallower—typically only 10% of those in the atmosphere. By contrast, L in the ocean is twice that in the atmosphere. Hence the bulk stability parameter D/L in the ocean is only 5% of that in the atmosphere and conditions are less convective, or, equivalently, less of the oceanic mixed layer is dominated by convection. This is shown schematically in Fig. 21 (adapted from Nicholls and Readings, 1979) where the four quadrants of the space z/D versus z/L are categorized based on the dominant dynamics. Diagonal lines are drawn for several values of D/L. Nicholls and Readings (1979) showed that data from the atmospheric mixed layer over water often fall into the upper left quadrant, where both wind stress and buoyancy forcing are important for $D/L < 10$. For the majority of data from the ring, D/L is between 3 and 9, while for the majority of data from the Bahamas, D/L is between 5 and 25. By contrast, for the Minnesota Experiment, most of the data fall in the range $30 < D/L < 200$.

Convective mixed layer scaling is expected to apply only when the turbulence is in equilibrium with the surface forcing. This restriction can be checked by comparing the convective time scale, $T_* \equiv D/W_*$, with the time scale of the forcing T_f. The T_* is the time required for a parcel at the surface to reach the base of the mixed layer while traveling in a convective plume. When T_f/T_* is high, the turbulence should be in equilibrium with the forcing. In the ocean, W_* is only 1% of that in the atmosphere and, since D is only a factor of ten smaller, T_* is ten times greater. Thus, the oceanic mixed layer responds much more slowly to changes in forcing (1 to 2 hours for D of 100 to 200 m) and is less likely to remain at equilibrium.

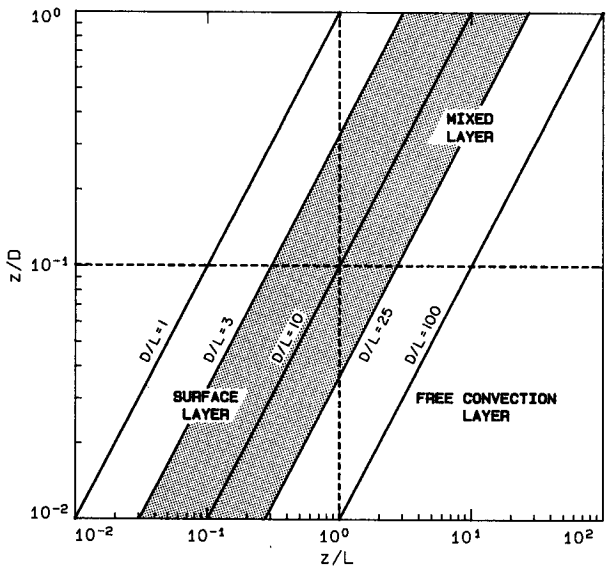

FIG. 21. Schematic diagram of regions of dominant dynamics in a turbulent boundary layer forced by shear stress and buoyancy flux. Most of the oceanic data are bounded by $D/L = 3$ and $D/L = 25$ (shaded) while the atmospheric values are much higher.

The atmospheric convective mixed layer is forced by the diurnal heating cycle, so T_f is a few hours. Since T_* is only 7 to 12 minutes and T_f/T_* is 16 to 25, many cycles can be completed before significant changes occur in the forcing and the turbulence can remain at equilibrium. In the ring, the forcing, J_b^0, remained high for more than a day during the cold air outbreak, so T_f may be taken as 1 day. Since T_* is 1 to 2 hours, T_f/T_* is 14 to 23—in the same range as in the atmosphere. In the Bahamas, the forcing is again diurnal, so T_f is a few hours. But T_* is a little over an hour, and just a few cycles may be completed before the mixed layer experiences significant changes in forcing. Thus, it is not obvious that the turbulence would be able to remain at equilibrium. This result suggests that the equilibrium assumption is not very restrictive; i.e., as long as a few mixed layer cycles can be completed before the forcing changes significantly, the mixed layer dissipation behaves as expected in a convective system.

We have shown that a useful parameterization of the mean dissipation rate in a convective mixed layer can be found by measuring J_b^0. This parameterization applies only to mean values of ϵ, however, since individual profiles often differ dramatically. Also, the zone of influence of other processes such as wave-driven turbulence and Langmuir circulation may be a considerable fraction of the mixed layer depth (Kitaigorodski et al., 1983; Thorpe, 1984; Thorpe, 1985). If the surface waves are large, the whole mixed layer may be dominated by processes other than convection, regardless of D/L. Finally, these results apply to existing mixed layers. The two mixed layers studied reached the depths they did because of weak background stratification. Each night in the Bahamas the diurnal mixed layer quickly penetrated through the weakly restratified remnant of the previous night's mixed layer. In the ring the stratification of the upper 150 m was weakened by some other process before the cold air outbreak. This is common among other oceanic convective systems that have been studied; in both the Mediterranean and Labrador Seas (Anati and Stommel, 1970; Clarke and Gascard, 1983; Gascard and Clarke, 1983), a preconditioning of the upper ocean results in weak stratification and makes possible convection under sudden cooling.

Acknowledgments. We thank Dale Hirt, Norge Larson, Matt Nicholas, Wayne Nodland, Eric Kunze and Pat McKeown for valuable assistance in collecting the

data. Wayne Nodland deserves special thanks for rebuilding a set of slip rings during a storm on the ring cruise; without his efforts, the experiment would have been a failure. This work was funded by the Office of Naval Research and the Naval Ocean Research and Development Activity.

APPENDIX

Data Processing Details

For isotropic turbulent flows, the viscous dissipation rate is given by

$$\epsilon = 7.5\nu\overline{\left[\frac{\partial u_1'}{\partial x_3}\right]^2} \quad [\mathrm{W\,kg^{-1}}] \qquad \text{(A1)}$$

where ν is the kinematic viscosity and u_1' is the cross-stream velocity perturbation. The variance of the gradients is computed by integrating spectra so noise can be excluded from the estimates and corrections can be made for the response functions of the sensors and electronics:

$$\epsilon = 7.5\nu\int_{k_0}^{k_c}(2\pi k)^2 E_n(k)\,dk \qquad \text{(A2)}$$

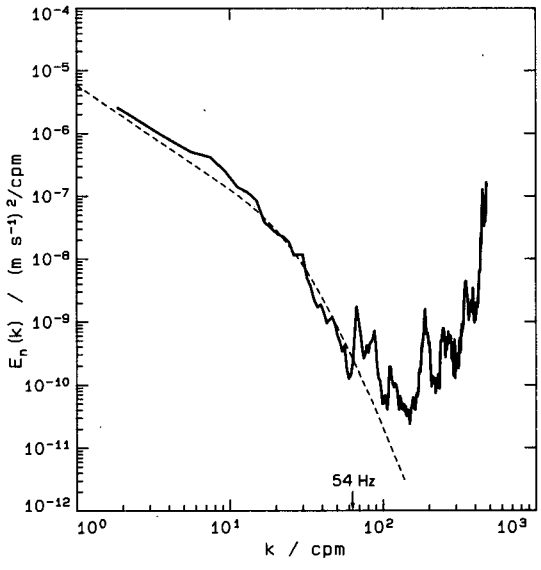

FIG. A1. Typical small-scale velocity spectrum from one of the lift probes. Mechanical and electrical vibration peaks begin to contaminate the spectrum at frequencies near 55 Hz. The integrations of velocity spectra are always terminated before 54 Hz (arrow, the beginning of the vibration peak) to avoid including noise in the estimates of ϵ. The dashed line is the Nasmyth spectrum (Nasmyth, 1970) for the ϵ given by the data spectrum ($\epsilon = 1.52 \times 10^{-7}$ W kg^{-1}). Termination of the spectra at 54 Hz begins to result in significant underestimates of ϵ for $\epsilon > 10^{-6}$ W kg^{-1}.

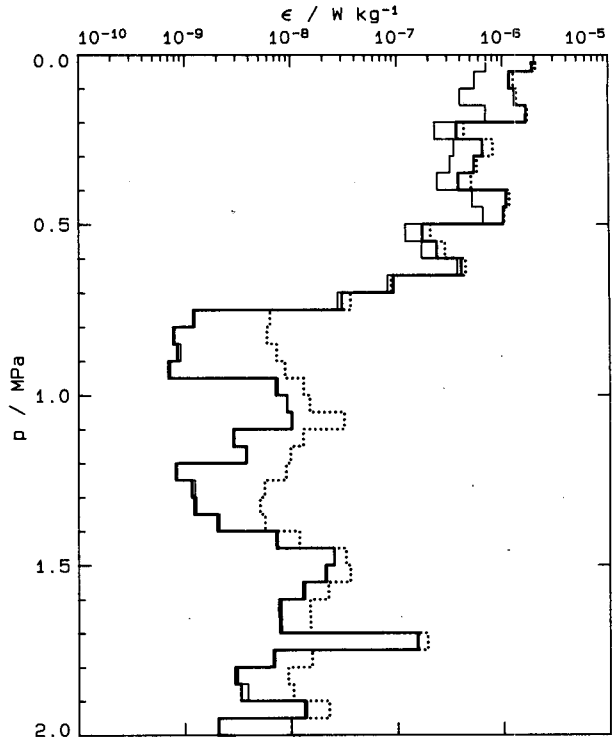

FIG. A2. Comparison of the effect on ϵ of varying f_c, the integration cutoff frequency. Three cases are shown: f_c = 54 Hz (dotted line), f_c = 15 Hz (thin solid line), and a variable f_c based on the universal cross-stream turbulent velocity spectra (thick solid line). In the turbulent mixed layer ($p < 0.7$ MPa), the variable cutoff and f_c = 54 Hz give similar results, while below the mixed layer ($p > 0.7$ MPa) the variable cutoff and f_c = 15 Hz agree closely. These results are consistent with an examination of individual spectra, and the variable cutoff method was adopted as standard.

where E_n is the spectrum of cross-stream velocity fluctuations, and k_0 is the lowest nonzero Fourier wavenumber ($k_0 \approx 1.2$ cpm). Determining the upper bound for the integration (k_c) is a compromise between excluding the noise and resolving the signal variance. Since hundreds of spectra are computed to produce a dissipation profile, k_c must be estimated automatically.

Determining k_c is difficult because the spectral noise level is not well defined and the data are prone to contamination by mechanical vibrations and electrical noise. For example, all the velocity spectra (for $\epsilon < 5 \times 10^{-6}$ W kg^{-1}) have a broad mechanical vibration peak (Fig. A1) centered near 70 Hz (140 cpm at a fall rate of 0.5 m s^{-1}). Thus, the integrations must be terminated before the noise peak. Two procedures have been used and compared. The first was simply to terminate all integrations at a fixed frequency. The obvious disadvantage of this method is that to avoid making gross overestimates of the lowest values of ϵ, f_c must be so low that moderate to high ϵ is underestimated.

The second method is based on the resemblance of many of the velocity spectra to a "universal" spectral form for cross-stream velocity in the dissipation range (Nasmyth, 1970; Oakey, 1982). To use the method, each data spectrum is integrated to 10 cpm; the resulting value is called ϵ_{10}. The cutoff wavenumber is then calculated using the universal spectrum by the following procedure: calculate the predicted total dissipation rate, ϵ_p, from a universal spectrum having the same ϵ_{10} [using a polynomial function, $p_1(\epsilon_{10})$]; compute the wavenumber, k_{90}, at which 90% of ϵ_p is resolved in the universal spectrum (another polynomial function, $p_2(\epsilon_p)$ is used); if $k_{90} < 54$ W integrate to k_{90}, otherwise integrate to 54 W.

The results of applying these two methods for a single profile are shown in Fig. A2. The fixed cutoff method was used with cutoff frequencies of 15 and 54 Hz. These frequencies were chosen since 15 Hz is the approximate cutoff frequency of the lowest signals and 54 Hz is the beginning of the mechanical vibration peak. In the mixed layer, the variable cutoff method and fixed cutoff method with $f_c = 54$ Hz agree to within an rms difference of 12.5%, while using $f_c = 15$ Hz gives an rms difference of 40%. In the quieter region below the mixed layer, using $f_c = 54$ Hz gives gross overestimates, and the rms difference between the two methods is more than 400%. Using $f_c = 15$ Hz, however, gives results that agree to within an rms difference of 5%.

The universal spectrum method was chosen for all ϵ profiles shown in previous chapters since it behaves well in both active and quiet sections of the water column. The size of the underestimate of ϵ caused by terminating the integration at 54 Hz can be estimated based on the universal spectra. For typical mixed layer values $\epsilon = 10^{-7}$ W kg^{-1} and $W = 0.65$ m s^{-1}, the integration cutoff scheme introduces an underestimate of <5%; for the maximum mixed layer values of $\epsilon = 10^{-6}$ W kg^{-1}, the underestimate is about 10%.

REFERENCES

Anati, D., and H. Stommel, 1970: The initial phase of deep water formation in the Northwest Mediterranean during MEDOC '69. *Cah. Oceanogr.* **22,** 343–352.

Atlas, D., S. H. Chou and W. P. Byerly, 1983: The influence of coastal shape on winter mesoscale air–sea interaction. *Mon. Wea. Rev.*, **111,** 245–252.

Baker, M. A., and C. H. Gibson, 1986: Sampling turbulence in the stratified ocean: statistical consequences of strong intermittency. Submitted to *J. Phys. Oceanogr.* (In press).

Businger, J. A., J. C. Wyngaard, Y. Izumi and E. F. Bradley, 1971: Flux-profile relationships in the atmospheric surface layer. *J. Atmos. Sci.*, **28,** 181–189.

Caughey, S. J., and S. G. Palmer, 1979: Some aspects of turbulence structure through the depth of the convective boundary layer. *Quart. J. Roy. Meteor. Soc.*, **105,** 811–827.

Chambers, J. M., W. S. Cleveland, B. Kleiner and P. A. Tukey, 1983: *Graphical Methods for Data Analysis.* Duxbury Press, 395 pp.

Chou, S. H., and D. Atlas, 1982: Satellite estimates of ocean-air heat fluxes during cold air outbreaks. *Mon. Wea. Rev.*, **110,** 1434–1450.

Clarke, R. A., and J. C. Gascard, 1983: The formation of Labrador Sea Water. Part I: Large-scale processes. *J. Phys. Oceanogr.*, **3,** 185–196.

Deardorff, J. W., 1972: Numerical Investigation of neutral and unstable planetary boundary layers. *J. Atmos. Sci.*, **29,** 91–115.

Denman, K. L., and M. Miyake, 1973: Upper layer modification at Ocean Station Papa: observations and simulations. *J. Phys. Oceanogr.*, **3,** 185–196.

Drever, R. G., and T. B. Sanford, 1980: An expendable temperature and velocity profiler (XTVP). *Proc. Near-Surface Ocean Experimental Technology Workshop,* Bay St. Louis, MS, Naval Ocean Research and Development Activity, 163–173.

Efron, B., and G. Gong, 1983: A leisurely look at the bootstrap, the jackknife, and cross-validation. *Amer. Statist.*, **37,** 36–48.

Elliott, J. A., and N. S. Oakey, 1980: Average microstructure levels and vertical diffusion for Phase III GATE. *Deep-Sea Res., GATE-1 Suppl.*, **26,** 273–294.

Gascard, J. C., and R. A. Clarke, 1983: The formation of Labrador Sea Water. Part II: Mesoscale and smaller-scale processes. *J. Phys. Oceanogr.*, **3,** 1779–1797.

Gill, A. E., 1982: *Atmosphere-Ocean Dynamics.* Academic Press, 662 pp.

Gregg, M. C., C. S. Cox and P. W. Hacker, 1973: Vertical microstructure measurements in the central North Pacific. *J. Phys. Oceanogr.*, **3,** 458–469.

——, W. E. Nodland, E. E. Aagaard and D. H. Hirt, 1982: Use of a fiber-optic cable with a free-fall microstructure profiler. *Oceans '82 Conf. Record.* Washington, D.C., Mar. Technol. Soc., 260–265.

——, E. A. D'Asaro, T. J. Shay and N. G. Larson, 1986: Observations of persistent mixing and near-inertial internal waves. *J. Phys. Oceanogr.*, **16,** 856–885.

Guillemet, B., H. Isaka and P. Mascart, 1983: Molecular dissipation of turbulent fluctuations in the convective mixed layer. Part I: Height variations of dissipation rates. *Bound.-Layer Meteor.*, **27,** 141–162.

Gurvich, A. S., and A. M. Yaglom, 1967: Breakdown of eddies and probability distributions for small-scale turbulence. *Phys. Fluids,* **10**(Suppl.), S59–S65.

Imberger, J., 1985: The diurnal mixed layer. *Limnol. Oceanogr.*, **30,** 737–770.

Joyce, T. M., and M. C. Stalcup, 1985: Wintertime convection in a Gulf Stream warm-core ring. *J. Phys. Oceanogr.*, **15,** 1032–1042.

Kaimal, J. C., J. C. Wyngaard, D. A. Haugen, O. R. Coté, Y. Izumi, S. J. Caughey and C. J. Readings, 1976: Turbulence structure in the convective boundary layer. *J. Atmos. Sci.*, **33,** 2152–2169.

Kitaigorodski, S. A., M. A. Donelan, J. L. Lumley and E. A. Terray, 1983: Wave-turbulence interactions in the upper ocean. Part II: Statistical characteristics of wave and turbulent components of the random velocity field in the marine surface layer. *J. Phys. Oceanogr.*, **13,** 1988–1999.

Kunze, E., 1986: The mean and near-inertial wave velocity fields in a warm-core ring. *J. Phys. Oceanogr.*, **16,** 1444–1461.

Large, W. G., and S. Pond, 1981: Open ocean momentum flux measurements in moderate to strong winds. *J. Phys. Oceanogr.*, **11,** 324–336.

——, and ——, 1982: Sensible and latent heat flux measurements over the open ocean. *J. Phys. Oceanogr.*, **12,** 446–462.

Larson, N. G., and M. C. Gregg, 1983: Turbulent dissipation and shear in thermohaline intrusions. *Nature,* **306,** 26–32.

Moum, J. N., and R. G. Lueck, 1985: Causes and implications of noise in oceanic dissipation measurements. *Deep-Sea Res.*, **32,** 379–390.

Nasmyth, P., 1970: *Oceanic Turbulence.* Ph.D. dissertation, Institute of Oceanography, University of British Columbia, 69 pp.

Nicholls, S., and C. J. Readings, 1979: Aircraft observations of the structure of the lower boundary layer over the ocean. *Quart. J. Roy. Meteor. Soc.*, **105,** 785–802.

Niiler, P. P., and E. B. Kraus, 1977: One-dimensional models of the upper ocean. *Modeling and Prediction of the Upper Layers of the Ocean,* E. B. Kraus, Ed., Pergamon, 143–172.

Oakey, N. S., 1982: Determination of the rate of dissipation of turbulent energy from simultaneous temperature and velocity shear microstructure measurements. *J. Phys. Oceanogr.*, **12,** 256–271.

——, and J. A. Elliott, 1982: Dissipation within the surface mixed layer. *J. Phys. Oceanogr.*, **12,** 171–185.

Osborn, T. R., 1978: Measurements of energy dissipation adjacent to an island. *J. Geophys. Res.*, **83,** 2939–2957.

——, and W. R. Crawford, 1980: An airfoil probe for measuring turbulent velocity fluctuations in water. *Air–Sea Interaction,* F. Dobson, L. Haase and R. Davis, Eds., Plenum, 369–386.

——, and R. G. Lueck, 1985: *J. Phys. Oceanogr.*, **15,** 1502–1520.

Phillips, O. M., 1977: *The Dynamics of the Upper Ocean.* Cambridge University Press, 336 pp.

Shay, T. J., 1985: *Convectively-Driven Turbulent Mixing in the Upper Ocean.* Ph.D. dissertation, University of Washington, 89 pp.

——, and M. C. Gregg, 1982: Measurements in a convective mixed layer. *Eos Trans., Amer. Geophys. Un.*, **63,** No. 45, 1002(abstract).

——, and ——, 1984a: Turbulence in an oceanic convective mixed layer. *Nature,* **310,** 282–285.

——, and ——, 1984b: Turbulence in an oceanic convective mixed layer (Corrigendum). *Nature,* **311,** 84.

Smith, S. D., and F. W. Dobson, 1984: The heat budget at Ocean Weather Ship Bravo. *Atmos.-Ocean,* **22,** 1–22.

Thorpe, S. A., 1984: On the determination of K_v in the near-surface ocean from acoustic measurements of bubbles. *J. Phys. Oceanogr.*, **14,** 855–863.

——, 1985: Small-scale processes in the upper ocean boundary layer. *Nature,* **318,** 519–522.

Washburn, L., and C. H. Gibson, 1984: Horizontal variability of temperature microstructure at the base of a mixed layer during MILE. *J. Geophys. Res.*, **89,** 3507–3522.

Wyngaard, J. C., 1983: Lectures on the planetary boundary layer. *Mesoscale Meteorology—Theories, Observations and Models,* D. K. Lilly and T. Gal-Chen, Eds., 603–650.